

# Multiple, coeval silicic magma storage domains beneath the Laguna Del Maule volcanic field inferred from gravity investigations

Sarah F Trevino<sup>1</sup>, Craig Andrew Miller<sup>2</sup>, Basil Tikoff<sup>3</sup>, Dominique Fournier<sup>4</sup>, and Bradley S Singer<sup>3</sup>

<sup>1</sup>University of Wisconsin - Madison

<sup>2</sup>GNS Science

<sup>3</sup>University of Wisconsin-Madison

<sup>4</sup>Mira Geoscience

November 21, 2022

## Abstract

The rhyolite-producing Laguna del Maule volcanic field (LdMVF) records magma-induced surface inflation rates of  $\sim 25$  cm/year since 2007. During the Holocene,  $\sim 60$  meters of cumulative surface uplift is recorded by paleoshorelines of the Laguna del Maule, located on the southeast edge of the LdMVF (Chile-Argentina border) near the Barrancas volcanic complex. Rhyolites from the Barrancas complex erupted over  $\sim 14$  ka including some of the youngest ( $1.4 \pm 0.6$  ka) lava flows in the field. New gravity data collected on the Barrancas complex reveals a Bouguer low ( $-6$  mGal, Barrancas anomaly) that is distinct from the pronounced gravity low ( $-19$  mGal; Lake anomaly) associated with present-day deformation and magma intrusion to the north. Three-dimensional inversion of the Barrancas anomaly indicates the presence of a magma body with a maximum density contrast of  $-250$  kg/m<sup>3</sup> centered at a depth of  $\sim 3$  km below surface. Comparison of model densities with measured densities from nearby silicic plutons suggest that a magma body, containing  $< 30$  % melt phase and a low volatile content, exists beneath the Barrancas complex. The Barrancas and Lake gravity lows represent magma in different physical states, associated with past and present-day storage beneath the LdMVF. The gravity model mirrors existing geochemical observations which independently indicate that at least two distinct rhyolites were generated and stored as discrete magma bodies within the broader LdMVF. Small temperature changes of these discrete bodies could reverse crystallization and viscous lock-up and propel magma toward a crystal-poor eruptible state.

1 Multiple, coeval silicic magma storage domains beneath the Laguna Del Maule volcanic field  
2 inferred from gravity investigations

3

4 **Sarah F. Trevino<sup>1</sup>; Craig A. Miller<sup>2</sup>; Basil Tikoff<sup>1</sup>; Dominique Fournier<sup>3</sup>; Brad S Singer<sup>1</sup>**

5 <sup>1</sup>Department of Geoscience, University of Wisconsin–Madison, Madison WI, 53706, USA

6 <sup>2</sup>GNS Science, Wairakei Research Centre, Taupo 3352, New Zealand

7 <sup>3</sup>Mira Geoscience, 512B 409 Granville St. Vancouver, BC V6C 1T2, Canada

8 Corresponding author: Craig Miller ([c.miller@gns.cri.nz](mailto:c.miller@gns.cri.nz))

9 **Key Points: (140 characters max)**

- 10
- At least two separate magma storage regions in different physical states exist beneath the
  - 11 Laguna del Maule volcanic field
  - 12 • A -6 mGal gravity anomaly below the Barrancas complex is close to a postulated
  - 13 inflation source which produced ~62 m of Holocene uplift
  - 14 • Comparing model densities to nearby plutons and seismic models indicates Barrancas
  - 15 magma is above solidus with a small melt proportion.

16

17

18

19 **Abstract**

20           The rhyolite-producing Laguna del Maule volcanic field (LdMVF) records magma-  
21 induced surface inflation rates of  $\sim 25$  cm/year since 2007. During the Holocene,  $\sim 60$  meters of  
22 cumulative surface uplift is recorded by paleoshorelines of the Laguna del Maule, located on the  
23 southeast edge of the LdMVF (Chile-Argentina border) near the Barrancas volcanic  
24 complex. Rhyolites from the Barrancas complex erupted over  $\sim 14$  ka including some of the  
25 youngest ( $1.4 \pm 0.6$  ka) lava flows in the field. New gravity data collected on the Barrancas  
26 complex reveals a Bouguer low ( $-6$  mGal, Barrancas anomaly) that is distinct from the  
27 pronounced gravity low ( $-19$  mGal; Lake anomaly) associated with present-day deformation and  
28 magma intrusion to the north. Three-dimensional inversion of the Barrancas anomaly indicates  
29 the presence of a magma body with a maximum density contrast of  $-250$  kg/m<sup>3</sup> centered at a  
30 depth of  $\sim 3$  km below surface. Comparison of model densities with measured densities from  
31 nearby silicic plutons suggest that a magma body, containing  $< 30$  % melt phase and a low  
32 volatile content, exists beneath the Barrancas complex. The Barrancas and Lake gravity lows  
33 represent magma in different physical states, associated with past and present-day storage  
34 beneath the LdMVF. The gravity model mirrors existing geochemical observations which  
35 independently indicate that at least two distinct rhyolites were generated and stored as discrete  
36 magma bodies within the broader LdMVF. Small temperature changes of these discrete bodies  
37 could reverse crystallization and viscous lock-up and propel magma toward a crystal-poor  
38 eruptible state.

39

40 **Plain Language Summary**

41       The Laguna del Maule volcanic field in Chile, has a long history of eruptions that  
42 produce large explosions and voluminous lava flows. Lava emitted during these eruptions comes  
43 from shallow sources of partially molten rock (magma) located a few kilometers below the  
44 surface. Magma intruded from below and into these shallow regions has caused extensive  
45 ground deformation around the lake over the last 10,000 years. To understand the causes of  
46 deformation and assess the likelihood of future eruptions, it is essential to know the location and  
47 present-day state of magma within the crust. Magma is typically less dense than the surrounding  
48 rock and these density variations cause small changes in the local gravity field, detectable with  
49 geophysical instruments. We collected a new set of gravity measurements at the Barrancas  
50 volcanic complex to determine if magma is present beneath the volcano that last erupted about  
51 two thousand years ago. Our data reveal a shallow magma body at depth beneath the Barrancas  
52 complex. This new magma body is separate from another magma body located in a different  
53 part of the Laguna del Maule volcanic field, which has important implications for the assessment  
54 of future volcanic hazards in the region.

55

56 **1 Introduction**

57       Snapshots of the geologic record showing the evolution of shallow silicic plutonic and  
58 magmatic systems through to their ultimate expression as explosive and effusive rhyolite  
59 eruptions are rare. Recent geochemical and geochronological studies (Glazner et al., 2004;  
60 Cooper & Kent, 2014; Barboni et al., 2016; Rubin et al., 2017; Andersen et al., 2017a; 2018;  
61 Schaen et al., 2017) of eruptive products and exhumed plutons propose that shallow silicic  
62 reservoirs exist as “mush” systems containing discrete batches of eruptible interstitial melt within  
63 a larger mostly crystalline framework (Bachmann & Bergantz, 2004; Hildreth, 2004). Over

64 time, these bodies may cool to form plutons or, with the addition of heat and volatiles delivered  
65 via basaltic to andesitic intrusions, melting or defrosting of the mush can rapidly produce  
66 eruptible pools of crystal-poor rhyolitic melt (Druitt et al., 2012; Cooper & Kent, 2014; Till et  
67 al., 2015; Andersen et al., 2018). These data and models propose a continuum between the end  
68 members of cold plutonic storage systems and systems that are heated and incubated such that  
69 they may produce explosive eruptions.

70 Geophysical imaging can provide insight into the location, geometry, and present state of  
71 silicic plutonic and magmatic systems (e.g., Magee et al., 2018). Seismic, magnetotelluric, and  
72 gravity surveys (Bachmann & Bergantz, 2008; Bertrand et al., 2012; Represas et al., 2012; del  
73 Potro et al., 2013; Comeau et al., 2015; Pritchard & Gregg, 2016; Gaynor et al., 2019; Paulatto et  
74 al., 2019) have imaged silicic plutonic and magmatic systems in a variety of tectonic settings,  
75 including at the LdMVF (Miller et al., 2017a; 2017b; Cordell et al., 2018; Weststad et al.,  
76 2019; Bai et al., 2020; Peterson et al., 2020). These studies inferred the present physical states of  
77 magma bodies from the distribution of material properties such as density, conductivity, P and S-  
78 wave velocities. However, crustal-scale geophysical models are inherently low resolution that  
79 homogenize and smear out anomalous rock volumes, making the petrologic hypothesis of  
80 individual melt lenses within the broader crystal matrix difficult to resolve.

81 The LdMVF comprises at least 40 km<sup>3</sup> of post-glacial (younger than 20 ka) rhyolite  
82 encircling a 20 x 16 km lake basin and is thus the largest such concentration of rhyolite erupted  
83 in the Andes (Hildreth et al., 2010). Relative to the goals of this study, the LdMVF is an  
84 exceptional natural laboratory owing to: (1) rapid rates of surface inflation of over 25 cm/year  
85 since 2007 (Feigl et al., 2014; Le Mével et al., 2015; 2016) that have re-accelerated recently (Le  
86 Mével et al., 2019), and more than 60 meters of surface warping during the Holocene (Singer et

87 al., 2018), that reflect active growth of a large underlying magma reservoir system (Singer et al.,  
88 2014), (2) The geochronology, petrology, and geochemistry of the LdMVF eruptive products are  
89 well documented with mineral compositions revealing at least two physically discrete,  
90 chemically distinct, long-lived rhyolite-producing domains in the upper crust (Andersen et al.,  
91 2017b; 2018; 2019), and melt inclusions indicating an H<sub>2</sub>O-rich, CO<sub>2</sub>-charged, magma reservoir  
92 system producing rhyolitic liquids from 14 to 4 km depth (Klug et al., 2020), and (3) The late  
93 Miocene Risco Bayo-Huemul plutonic complex, exposed only 20 km to the west, spans a  
94 compositional range of gabbro to high-silica granite very similar to the LdMVF and is of  
95 comparable dimensions to the LdMVF (Schaen et al., 2017; 2018; Garibaldi et al., 2019).

96 Here we expand the 3D density model of Miller et al. (2017b) to include new gravity data  
97 from the Barrancas complex (Sruoga et al., 2015; 2018) in the southern part of the Laguna del  
98 Maule volcanic field (LdMVF). Our observations reveal a previously unmapped -6 mGal  
99 Bouguer gravity anomaly below the Barrancas complex (“Barrancas anomaly”) that is physically  
100 independent of the larger (-19 mGal) negative anomaly associated with current surface inflation  
101 at LdMVF (“Lake anomaly”) (Le Mével et al., 2016; Miller et al., 2017b). We also report new  
102 density measurements from granites comprising the nearby Risco Bayo and Huemul plutons  
103 (Schaen et al., 2017) as a novel means of exploring the full density evolution of silicic magmas  
104 in this part of the Andes. Moreover, we interpret these new geophysical data in context of the  
105 extensive petrological (Andersen et al., 2017b, 2018, 2019; Cáceres et al., 2018; Klug et al.,  
106 2020) and geomorphic (Singer et al., 2018) findings from LdMVF. This multidisciplinary  
107 approach allows us to reduce the non-uniqueness inherent in geophysical models and to better  
108 understand the hazards posed by silicic magma systems (Till et al., 2018). Our high-resolution

109 geophysical observations of the broad magmatic system at LdMVF images multiple embedded  
110 magma bodies, in different developmental stages within a large silicic reservoir.

## 111 **2 Geologic setting and previous work**

112 The Laguna del Maule volcanic field (LdMVF) (Fig. 1), located on the crest of the Andes  
113 (36° S) within the Southern Volcanic Zone, comprises the region's largest concentration of  
114 crystal poor rhyolite and has hosted at least 50 post-glacial rhyolitic eruptions comprising >40  
115 km<sup>3</sup> since 25 ka (Andersen et al., 2017b; Hildreth et al., 2010). The LdMVF lies 20-30 km south  
116 east of the 7.2 to 6.2 Ma Risco Bayo and Huemul plutonic complexes (Schaen et al., 2017, 2018;  
117 Garibaldi et al., 2018). The Huemul pluton is a high silica granite that is inferred to reflect  
118 residual melt extracted from crystal cumulates (Schaen et al., 2017). These plutons are  
119 interpreted as frozen magma reservoirs that solidified at 4-6 km depth analogous to those that  
120 likely are growing beneath the present day LdMVF (Schaen et al. 2017; Le Mevel et al., 2016;  
121 Andersen et al., 2017b; 2018; Weststad et al., 2019). As such, they offer a unique perspective  
122 on how the LdMVF magmatic system has evolved that is complimentary to that derived solely  
123 from the eruptive products of the LdMVF.

124 Plagioclase and zircon petrochronologic data reveal that the two distinct eruptive  
125 episodes at 23-19 ka and 8–2 ka also reflect rhyolite generation in compositionally and  
126 physically distinct domains beneath the LdMVF (Andersen et al., 2018; 2019). The four  
127 youngest vents and eruptive complexes are in the south and eastern part of the LdMVF,  
128 suggesting that this region once contained a significant volume of eruptible melt. The youngest  
129 eruptions, dated by <sup>40</sup>Ar/<sup>39</sup>Ar methods or inferred from geomorphology, are the Cari Launa (<3.3  
130 ±0.6 ka), the rhyolite of Colada Divisoria (2.1 ± 0.7 ka), Colada Las Nieblas (~1.8 ka), and the  
131 Barrancas complex (14.5-1.9 ka) (Andersen et al., 2017b, 2019). The Colada Las Nieblas flow

132 lacks pumice cover and displays an uneroded morphology and is considered of comparable age  
133 to the younger portions of the Barrancas complex and eastern Barrancas complex lavas (around  
134 2.1 to 1.9 ka). The  $^{40}\text{Ar}/^{39}\text{Ar}$  chronology is supported by  $^{36}\text{Cl}$  surface exposure dates of  $2.5 \pm 0.7$   
135 ka and  $1.4 \pm 0.6$  ka for the youngest Barrancas flows (Singer et al., 2018). In addition, the  
136 younger flow from the Cari Launa vent yields an imprecise  $^{36}\text{Cl}$  surface exposure date of  $0.8 \pm$   
137  $0.6$  ka, indicating a late Holocene age (Singer et al., 2018).

138 Within the LdMVF, the Barrancas volcanic complex is distinctive because it is the site of  
139 multiple dome forming episodes within the last 14 ka and contains some of the youngest ( $1.4 \pm$   
140  $0.6$  ka) erupted lavas of the LdMVF. Between 14.5 and 8.4 ka at the LdMVF, rhyolite erupted  
141 only from the Barrancas complex and eruptive material from Barrancas forms a large portion ( $\sim$   
142  $6 \text{ km}^3$ ) of the post Last Glacial Maximum eruptive history of LdMVF. The western Barrancas  
143 dome complex was constructed between 14.5 and 11.4 ka and partially collapsed to produce  
144 large block and ash flows that traveled  $\sim 13$  km filling valleys with deposits  $\sim 60 - 120$  m thick,  
145 decreasing to 10 m in distal areas (Fig. 1; Sruoga et al., 2015, 2018). The younger eastern domes  
146 ( $5.6$  to  $1.4$  ka) produced 8 obsidian flows and several tephra falls and pyroclastic flows. The  
147 Barrancas domes show the only evidence of shallow hydrothermal alteration in the LdMVF.  
148 Advanced argillic alteration has affected these domes, as well as block and ash flow deposits,  
149 suggesting that circulation of  $> 300$  °C hydrothermal fluids may have contributed to dome  
150 collapse (Sruoga et al., 2018).

151 The Barrancas rhyolites are distinguished from the older 22-19 ka rhyolites erupted in the  
152 north from a magma source coincident with the Lake gravity anomaly by their elevated Sm and  
153 Y abundances, low  $\text{TiO}_2$  in magnetite, and high Ce in plagioclase crystals (Andersen et al.,  
154 2017b; 2018; 2019; Klug et al., 2020). The Barrancas rhyolites show no evidence for having

155 mixed with other spatially discrete rhyolites, strongly suggesting compartmentalization of  
156 eruptible domains within the wider magma reservoir (Andersen et al., 2018; 2019).

157 Petrologic evidence from melt inclusion composition and entrapment pressures (Klug et  
158 al., 2020) suggests that crystal poor rhyolite melt beneath the LdMVF accumulated in the  
159 shallow crust (50 – 350 MPa, ~ 2 to 8 km depth) after ascending out of rhyodacitic mush at ~8 –  
160 14 km. The crystal poor rhyolite accumulation pressures derived from melt inclusions are at the  
161 lower end of those derived from analysis of amphibole crystals in the rhyodacites (Andersen et  
162 al., 2017b; Cáceres et al., 2018) that suggest crystallization pressures of 190 – 400 MPa. The  
163 voluminous rcb-py pyroclastic flow on the south flank of the Barrancas complex (Fig. 1) has  
164 some of the lowest melt inclusion derived pressures (50 – 150 MPa) from LdMVF, consistent  
165 with its origin via collapse of shallowly emplaced, and thoroughly degassed, endogenous and  
166 exogenous domes (Sruoga, et al., 2018; Klug et al., 2020).

167 The summit of the Barrancas complex is < 5 km south of a high stand paleoshoreline that  
168 formed when the lake was dammed by the Espejos rhyolite coulée at 19.0 ka and is inferred to  
169 have been a horizontal surface when the lake catastrophically drained at 9.4 ka. The present day  
170 paleoshore is uplifted 62 m in the southern part of the lake basin relative to the northern part.  
171 This pattern is consistent with surface warping produced by an inflating magma reservoir located  
172 below the southeastern portion of the lake basin, beneath the northern flank of the Barrancas  
173 complex (Singer et al., 2018).

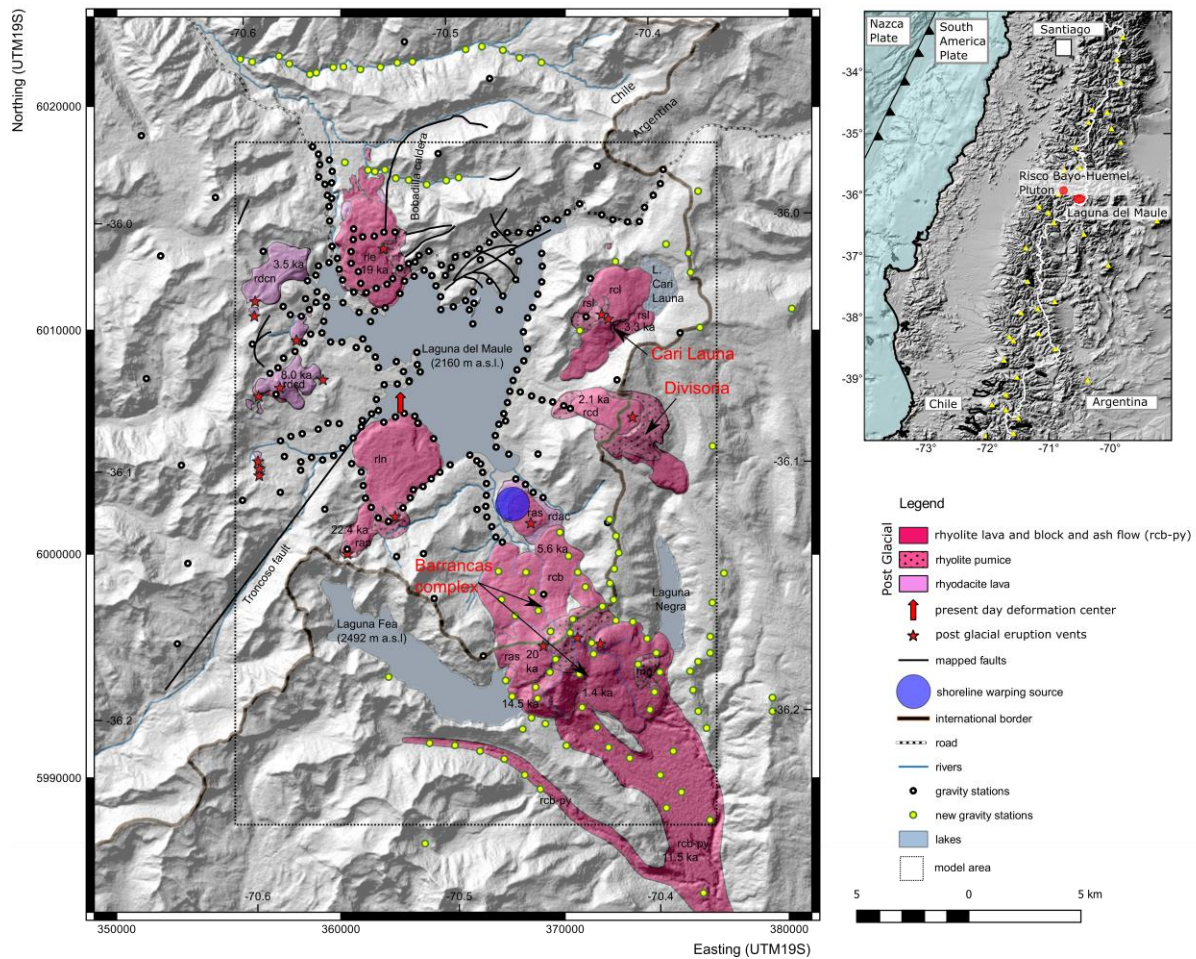
174 The identification of rapid surface inflation within the LdMVF, at rates greater than 25 cm/yr  
175 since 2007, has prompted several geophysical studies that have imaged a trans-crustal magma  
176 system and a small upper crustal fault system beneath the eponymous lake using teleseismic  
177 tomography (Bai et al., 2020), surface wave tomography (Wespestad et al., 2019), seismic

178 reflection and magnetics (Peterson et al., 2020), magnetotellurics (Cordell et al., 2018, 2019,  
179 2020), geodesy (Feigl et al., 2014; Le Mével et al., 2015, 2016; Zhan et al., 2019), and gravity  
180 (Miller et al., 2017b). Gravity inversion, teleseismic tomography, and surface wave tomography  
181 show overlapping low-density and low-velocity anomalies (referred to here as the “Lake”  
182 anomaly) interpreted as a crystal-rich, dacitic to rhyodacitic magma reservoir occupying between  
183 100 and 500 km<sup>3</sup> at depths between 2 and 12 km, containing domains including 20-70 km<sup>3</sup> of  
184 volatile-rich rhyolite melt that is spatially coincident with the deformation source. Teleseismic  
185 and surface wave tomography suggests that melt contents in the Lake magma body range from 5  
186 – 14 %, however these are likely to be minima due to inherent vertical smearing and wide grid  
187 cell widths (3 to 4 km) (Wespestad et al., 2019; Bai et al., 2020).

188 Teleseismic tomography (Bai et al., 2020) also resolves a low-V<sub>p</sub> anomaly in the southeast of  
189 the LdMVF beneath the Barrancas complex. This feature is elongated northeast-southwest, dips  
190 to the southwest, and is resolvable to about 25 km depth. The velocity perturbation of this  
191 feature is -100 to -200 m/s compared to -400 m/s for the main Lake anomaly. However, its  
192 location on the edge of the seismic array leads to greater uncertainty as to the geometry of this  
193 feature. Group velocity maps from surface wave tomography show a negative group velocity  
194 anomaly across the 0.29 to 0.39 Hz range in the southeast corner of the basin towards the  
195 Barrancas complex suggesting a melt phase may be present (Wespestad et al., 2019).

196 Using 3D MT inversion, Cordell et al. (2018, 2020) imaged the deeper portion of the magma  
197 system that extends north of the lake and likely represents a deep crustal zone of magma storage,  
198 mixing, and assimilation (Andersen et al., 2017b). The Barrancas complex is on the edge of the  
199 MT array, although there is a suggestion of a shallow (~1-3 km) conductive body (~10 Ωm)  
200 beneath Barrancas, below which (> 4 km) are more resistive rocks (> 100 Ωm).

201 Together the geophysical observations strongly point to a trans-crustal magma system  
 202 extending to within 2 km of the surface, which is consistent with the petrologic and geochemical  
 203 observations. Imaging of the Lake anomaly and identification and modeling of the source of  
 204 paleoshoreline warping prompted further geophysical investigation of the Barrancas complex,  
 205 which was on the edge of previous geophysical imaging campaigns.  
 206



207  
 208 **Figure 1.** Geological map of the Laguna del Maule volcanic field showing post glacial silicic lavas and pyroclastic  
 209 deposits. White dots are the gravity data from Miller et al. (2017b), yellow dots are new data from this study.  
 210 Modified from Miller et al. (2017b) and Andersen et al. (2017b).  
 211  
 212

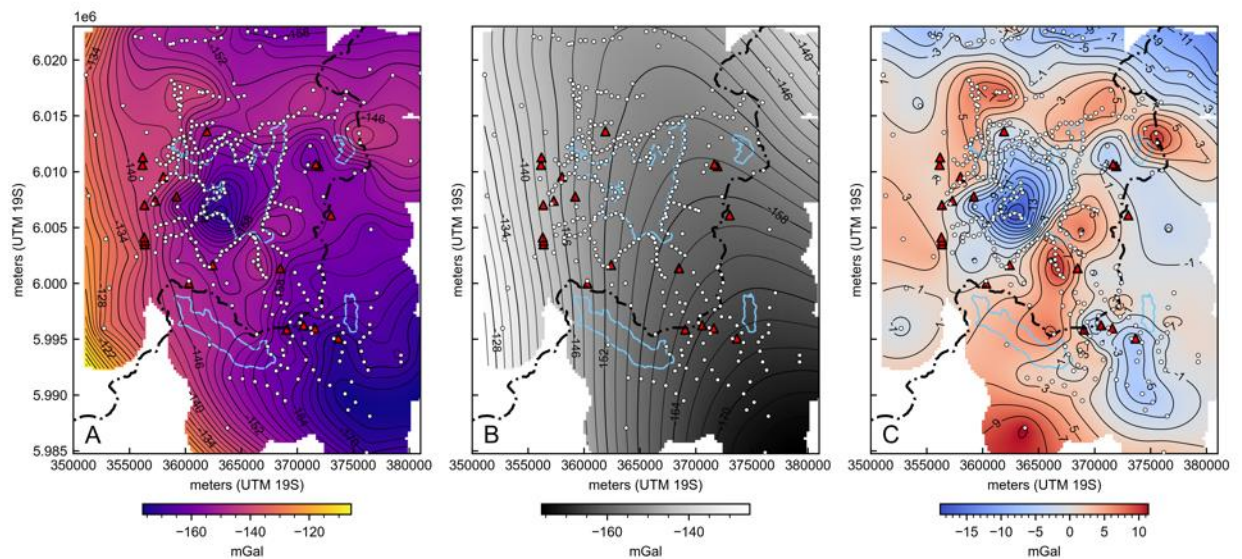
## 213 **3 Data**

### 214 **3.1 Gravity data**

215 We collected 105 additional terrestrial gravity measurements over two summer  
216 campaigns in December 2017 and March 2018, building on the work of Miller et al. (2017b)  
217 (Fig. 1). Measurements were taken every 500–1000 m in a series of 3–4 km long, radial and  
218 valley parallel profiles within a 15 km radius of the main Barrancas complex. Of the 105  
219 measurements, 19 were collected in two E-W transects in valleys north of the lake and four far-  
220 field gravity measurements were collected south and east into Argentina to improve the regional  
221 gravity field definition. For precise positioning we used a Leica 530 GPS receiver with 15-  
222 minute occupation time per station; with maximum baseline lengths of 10 km to the Observatorio  
223 Volcanológico de Los Andes del Sur (OVDAS) CGPS network in Chile, we obtain height errors  
224 of better than 15 cm ( $\sim 0.045$  mGal) at 95% confidence level.

225 Daily raw gravity data was corrected for Earth tide and drift using Gtools (Battaglia et al.,  
226 2012), to produce gravity values relative to the local base. Local gravity values were converted  
227 to absolute values using two nearby absolute gravity stations (Miller et al., 2017b). Gravity data  
228 were corrected to the ellipsoid height datum, as our heights are derived from GNSS  
229 measurements referenced to the WGS84 ellipsoid and follow the complete Bouguer anomaly  
230 data reduction scheme outlined in Hinze et al. (2005). Calculation of the reference density, which  
231 represents the average density of the crust above the reduction datum, using topographic  
232 correlation methods (Nettleton, 1939; Parasnis, 1966) yields densities of 2375 and 2361 kg/m<sup>3</sup>  
233 respectively. A similar analysis of a commercial dataset (Energy Development Corporation)  
234 from the nearby Mariposa geothermal prospect yields values of 2350 and 2452 kg/m<sup>3</sup>, while  
235 conversion of the OVDAS 1-D P-wave velocity model to density using the relationship of  
236 (Brocher, 2005), yields densities of 2429 to 2448 in the top 7 km. The average of all the density

237 determinations is  $2413 \text{ kg/m}^3$  that we approximate as  $2400 \text{ kg/m}^3$  for use in the gravity reduction.  
 238 Continental scale gravity models (Tašárová, 2007; Folguera et al., 2012) of the south-central  
 239 Andes, around latitude  $36^\circ\text{S}$  obtain an upper crustal density of  $2450 \text{ kg/m}^3$ , so our local scale  
 240 density values are similar to larger continental-scale values.



241 **Figure 2.** Gravity data collected at the Laguna del Maule volcanic field. A) Bouguer anomaly map, B) Second order  
 242 regional field, C) residual gravity anomaly. Red triangles are post-glacial eruption vents. The dot-dashed line is the  
 243 Chile – Argentina border and the lakes are outlined in light blue. Post-glacial eruption vents are red triangles, and  
 244 white dots are gravity station locations.  
 245

246

247 The new dataset was merged with the published (Miller et al., 2017b) gravity data to  
 248 produce an expanded Bouguer anomaly map of the LdMVF (Fig. 2). The new Bouguer anomaly  
 249 map identifies a gravity low on the southeast region of the LdMVF, spatially coincident with the  
 250 Barrancas complex and distinct from the gravity low beneath the lake (Fig. 2A). A second-order  
 251 polynomial fitted to the data (Uieda, 2018) (Fig. 2B) best approximates the measured regional

252 field gradient oriented approximately parallel to the South American/Nazca tectonic plate  
253 boundary and reflects the eastward dipping subducting plate. We removed the second-order  
254 polynomial from the Bouguer anomaly data to produce a residual gravity anomaly dataset  
255 suitable for inversion. Experiments with removing first- and third-order polynomials to  
256 approximate the regional field produce similar residual anomalies to the 2<sup>nd</sup> order, which we  
257 prefer as it is the lowest order surface that approximates the regional anomaly.

258 The new residual gravity map (Fig. 2C) shows the previously identified Lake anomaly  
259 (Miller et al., 2017b), as well as two more low gravity anomalies in the east of the field spatially  
260 associated with the Barrancas complex and Cari Launa vents. A -6 mGal anomaly is located on  
261 the southeastern flank of the Barrancas complex. The Barrancas anomaly consists of a small  
262 lobe located beneath the summit of the Barrancas eruption vents and the rest of the anomaly  
263 extends 5 km to the SE. The southern part of the Barrancas anomaly is broadly coincident with  
264 the location of a ~ 60 - 120 m thick valley filling block and ash flow deposit (Sruoga et al., 2015)  
265 that was emplaced south of the main volcanic domes and vents at 11.5 ka. It is possible that part  
266 of the gravity anomaly reflects this pyroclastic material which we investigate further in the  
267 discussion. A -3 mGal anomaly is associated with the Cari Launa and Divisoria vents, however  
268 it is not particularly well resolved as station coverage is sparser in this area.

### 269 **3.2 Density estimates from plutonic rocks**

270 Density measurements of plutonic intrusive rocks that represent an end member state of  
271 silica magma systems, are important to aid interpretation of densities derived from gravity  
272 models of silicic systems. Plutonic rocks are often inferred to represent the “frozen”, sub-solidus  
273 cumulates of magma reservoirs (Glazner et al., 2004; Bachmann et al., 2007). The 7.2-6.2 Ma,  
274 high silica granites in the Huemul pluton, located 30 km NW of the LdMVF, are interpreted to

275 be the frozen remnants of a once eruptible, crystal-poor, rhyolitic melt (Schaen et al., 2017;  
 276 2018). This melt is inferred to be extracted out of deeper residual mush at pressures of 100 to  
 277 200 MPa or about 3.7 to 7.2 km depth, but not necessarily erupted. This interpretation is  
 278 consistent with numerical models that consider crustal rheology, exsolved volatile contents, and  
 279 magma recharge which imply a narrow depth range, 6 to 8 km ( $200 \pm 50$  MPa), where silicic  
 280 magma reservoirs can incubate large bodies of potentially eruptible rhyolite (Huber et al., 2019).

281 Petrologic and structural studies of the Risco Bayo and Huemul plutons (Schaen et al.,  
 282 2017; 2018; Garibaldi et al., 2018) have revealed miarolitic cavities and rock fabrics indicative  
 283 of volatile and melt transport through an underlying crystal mush, including accumulation of  
 284 vapor bubbles at the roof of the reservoir. These observed features are similar to those proposed  
 285 to exist within the present-day magma body represented by the Lake anomaly (Miller et al.,  
 286 2017b; Andersen et al., 2018). As such, the geochemical composition and observed textures of  
 287 these exhumed granites make them an ideal, crystallized, end-member representative of a  
 288 present-day silicic melt storage system.

289 Direct density measurements of the high silica granites can be compared to geophysically  
 290 derived densities of the nearby silicic melt storage system at LdMVF to provide constraints for  
 291 interpreting the gravity anomalies. Density measurements were conducted using a glass  
 292 pycnometer on two to five specimens per intrusive unit of the Risco Bayo – Huemul plutonic  
 293 complex (Table 1).

294

Table 1: Density Measurements

<b>Geologic Unit</b>	<b>No. of Samples</b>	<b>Avg. density (kg/m<sup>3</sup>)</b>	<b>St. dev. (kg/m<sup>3</sup>)</b>	<b>SiO<sub>2</sub> content (Schaen 2018)</b>
Huemul high silica	5	2439	15	75-77

granite				
Huemul granite	5	2502	46	68-70
Risco Bayo granodiorite	5	2544	7	62-66
Huemul quartz. monzonite	5	2546	21	62-63
Risco Bayo microdiorite	5	2642	18	55
Risco Bayo gabbro	2	2699	-	51

295

296 We measured the densities of a suite of samples spanning the observed compositional range from  
 297 gabbro to high silica granite at the Risco Bayo and Huemul plutonic complex. The density range  
 298 varies by  $260 \text{ kg/m}^3$  reflecting the density increase from high silica granite to silica poor gabbro.  
 299 Samples from the Huemul high silica granite - which is interpreted to be the solidified analog of  
 300 a crystal poor, high silica melt extracted from the granite cumulate framework - have an average  
 301 density of  $2439 \text{ kg/m}^3 \pm 15 \text{ kg/m}^3$ . Density measurements of high silica granite samples that  
 302 contain miarolitic cavities varied by  $< 10 \text{ kg/m}^3$  from cavity free samples. As we only sampled a  
 303 fraction of the entire pluton, it is possible there are regions with greater cavity abundance that  
 304 could more significantly lower the density of the high silica granite. The samples representing  
 305 the cumulate residual phase have an average density of  $2502 \text{ kg/m}^3 \pm 46 \text{ kg/m}^3$ . The Bouguer  
 306 correction density of  $2400 \text{ kg/m}^3$  means that if plutonic rocks, such as found are Risco Bayo and  
 307 Huemul plutons, are present within the survey area, they should create a small positive gravity  
 308 anomaly.

#### 309 **4 Gravity Inversion Method**

310 To determine the density distribution within the subsurface, we developed a 3D inversion  
 311 model using a Gauss-Newton, gradient-based approach, implemented in the open source  
 312 SimPEG framework (Cockett et al., 2015). We implement a mixed  $L_p$  norm inversion scheme,  
 313 with a summary described below.

314 We construct a 3D mesh with 250 x 250 m horizontal cell size, with vertical cell size  
 315 increasing by a factor of 1.2 from 100 m in the top 500 m, to 420 m at the base of the grid at -  
 316 7000 m a.s.l., resulting in 451935 cells. We added 5 layers of padding cells in the horizontal  
 317 dimensions outside the data coverage to reduce edge effects. The mesh covers a subset of the  
 318 Bouguer gravity anomaly where the station density is highest, using 306 of the 342 stations  
 319 (rectangular box in Figure 1). Note that there is no interpolation of data in the inversion routine,  
 320 only the measured gravity data are used.

321 As proposed by (Tikhonov & Arsenin, 1977), the inverse problem can be formulated as  
 322 an optimization problem of the form:

$$323 \quad \phi(\mathbf{m}) = \phi_d(\mathbf{m}) + \beta\phi_m(\mathbf{m})$$

324 where  $\beta$  is the tradeoff or Tikhonov parameter. A small  $\beta$  results in a model that fits the data  
 325 very well but may include excessive structure so that  $\phi_m(\mathbf{m})$  is large. Conversely if  $\beta$  is large, the  
 326 optimization results in a large  $\phi_d(\mathbf{m})$ . The optimization is nonlinear, so a gradient-based, Gauss-  
 327 Newton method is used. To run the inversion, we search for a perturbation of the model that  
 328 reduces the objective function. The iterative optimization process continues until the algorithm  
 329 converges to a minimum and the misfit tolerance is achieved.

330 The optimal solution is found at the minimum of the objective function  $\phi_m(\mathbf{m})$  which is  
 331 made up of two terms: 1) The data misfit; and 2) The regularization scheme. Data misfit is a  
 332 metric which measures the difference between observed and predicted data. The regularization  
 333 is a metric that is constructed to evaluate the model's agreement with assumptions and prior  
 334 knowledge. We define the data misfit of the model  $\phi_d(\mathbf{m})$  as:

$$335 \quad \phi_d(m) = \frac{1}{2} \|\mathbf{W}_d(F[m] - \mathbf{d}_{obs})\|_2^2$$

336 where  $\mathbf{d}_{obs}$  is the observed data,  $\mathbf{F}[m]$  is a forward model that produces predicted data, and  $\mathbf{Wd}$   
 337 is a diagonal matrix with elements equal to  $\mathbf{Wd}_{ii} = 1/E$  where  $E_{ii}$  is the standard deviation of the  
 338  $i$ th data point. We set  $E$  to 0.1 mGal for our model.

339 The second element is the regularization function. With any inverse technique choice of  
 340 regularization parameters, it is important to control the final form of the model. Regularizations  
 341 can be tuned to produce smooth or compact models depending on the prior knowledge of the  
 342 interpreter. We follow the procedure of Fournier and Oldenburg (2019) such that sparsity  
 343 assumptions are introduced through a Scaled Iteratively Re-weighted Least Squares (S-IRLS)  
 344 method. The regularization function reduces to weighted least-squares problem of the form:

$$345 \quad \phi_m = \sum_{i=u,v,w} \sum_{j=s,x,y,z} \alpha_{ij} \left\| \mathbf{W}_i \mathbf{R}_{ij} \mathbf{D}_{ij} \mathbf{P}_i \mathbf{m} \right\|_2^2$$

346 where the projection matrices  $\mathbf{P}_i$  select individual component of the vector model. The gradient  
 347 terms  $\mathbf{D}_x, \mathbf{D}_y, \mathbf{D}_z$  are finite difference operators measuring the model roughness along the three  
 348 Cartesian directions, and  $\mathbf{D}_s$  is simply the identity matrix. Hyperparameters  $\alpha_j$  allow the user to  
 349 change the relative influence of each term.

350 Sparsity weights  $\mathbf{R}_j$  are calculated as:

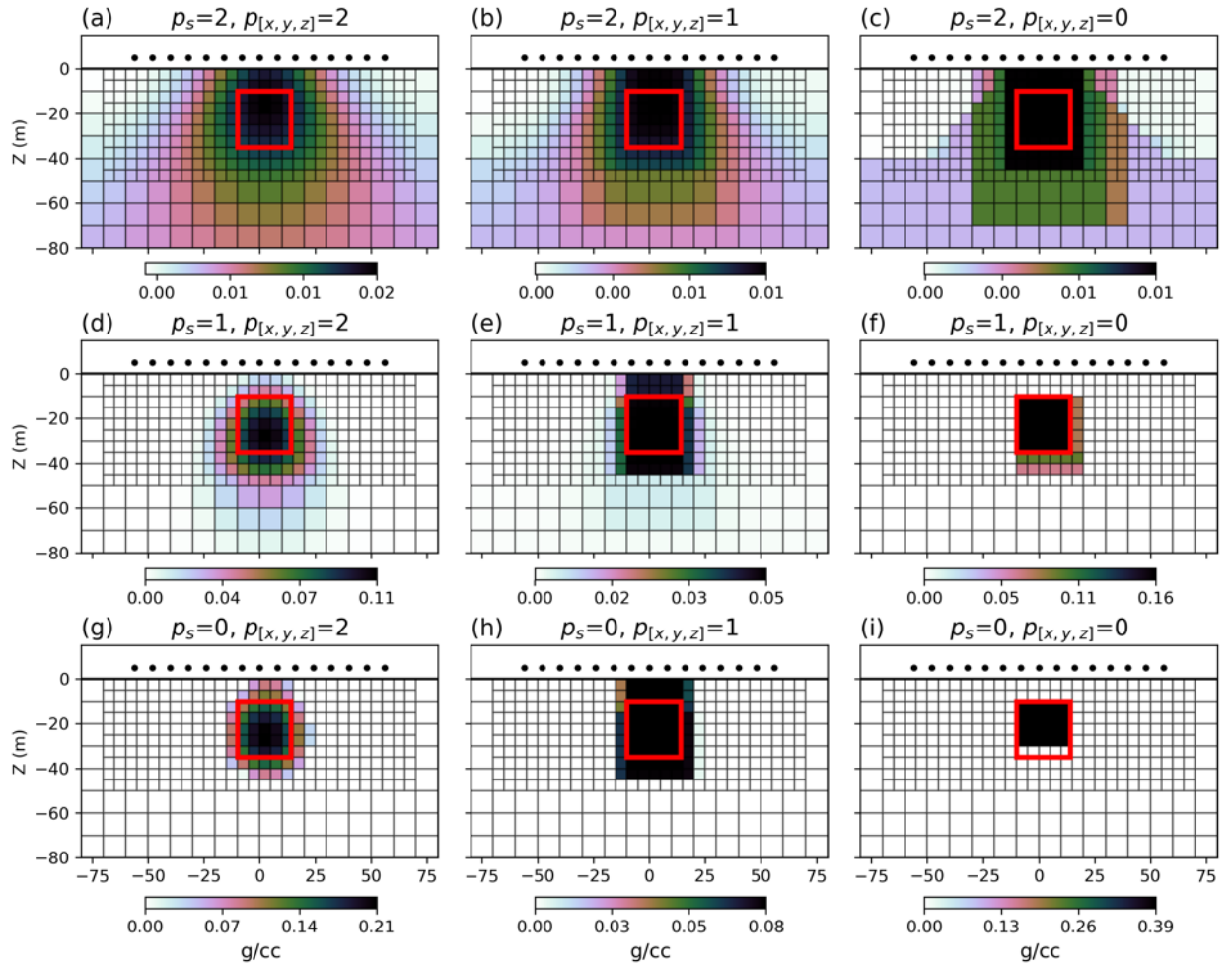
$$351 \quad \mathbf{R}_j \text{diag} = \gamma_j \left[ \left( (\mathbf{D}_j \mathbf{m}^{(k-1)})^2 + \epsilon_j^2 \right)^{p_j/2-1} \right]^{1/2}$$

352 such that weights depend on the model obtained at a previous  $k^{\text{th}}$  iteration. The  $\gamma_j$  scaling  
 353 parameters are used to balance the contribution of different  $\mathbf{l}_p$ -norm based on the maximum  
 354 derivatives. This regularization function is flexible and allows us to explore a range of possible  
 355 solutions by varying the  $\mathbf{P}_j$  values, where  $0 \leq p \leq 2$ . Our regularization norm is made up of four

356 terms, the first term represents the amplitude (density) and the second to fourth terms, the 3  
357 directional gradients.

358 Instead of deciding on a single regularization we choose to implement many, using all  
359 combinations of  $l_p$ . We then combine the models into a single median model. In our workflow,  
360 we run a twostep inversion process, firstly inverting the data with a 'smooth' constraint imposed  
361 with a  $L_2$  norm. Secondly, we compute a range of models using a  $l_p$  norm, where  $0 \leq p \leq 2$ . 0  
362 creates compact models while 2 creates smooth models, and 1 is intermediate. For our modeling  
363 we keep the 3 gradient terms equal and vary the amplitude term to create 9 possible models with  
364 norms [0,0,0,0], [0,1,1,1], [0,2,2,2], [1,0,0,0], [1,1,1,1], [1,2,2,2], [2,0,0,0], [2,1,1,1], [2,2,2,2].  
365 For example, the regularization [0111] places a 0 norm on the density amplitude and 1 norms on  
366 the three amplitude gradients. We then calculate the median model from the complete suite of  
367 models. This approach also allows us to calculate the probability of a density value occurring in  
368 a model cell, importantly providing a method of assessing uncertainty of the model.

369 Figure 3 illustrates the effect of the different inversion norms on the model. Note that all  
370 the models fit the data within the error of the data. From this range of models, we calculate the  
371 median model and use the model ensemble to calculate the probability of a density value  
372 occurring in each cell.



373

374

375

376

377

378

**Figure 3.** Illustration of different model norms on the final model from a synthetic dataset. The input model outline is shown by the red square and has a density contrast of 0.4 g/cc. The top row (a-c) show norms with a smooth amplitude constraint i.e. [2,2,2,2], [2,1,1,1], [2,0,0,0]. The middle row (d-f) shows models with an intermediate amplitude constraint, i.e. [1,2,2,2], [1,1,1,1], [1,0,0,0] and the bottom row (g-i) shows models with a compact amplitude constraint, i.e. [0,2,2,2], [0,1,1,1], [0,0,0,0].

379

## 5 Inversion Model Results and Uncertainty

380

381

382

383

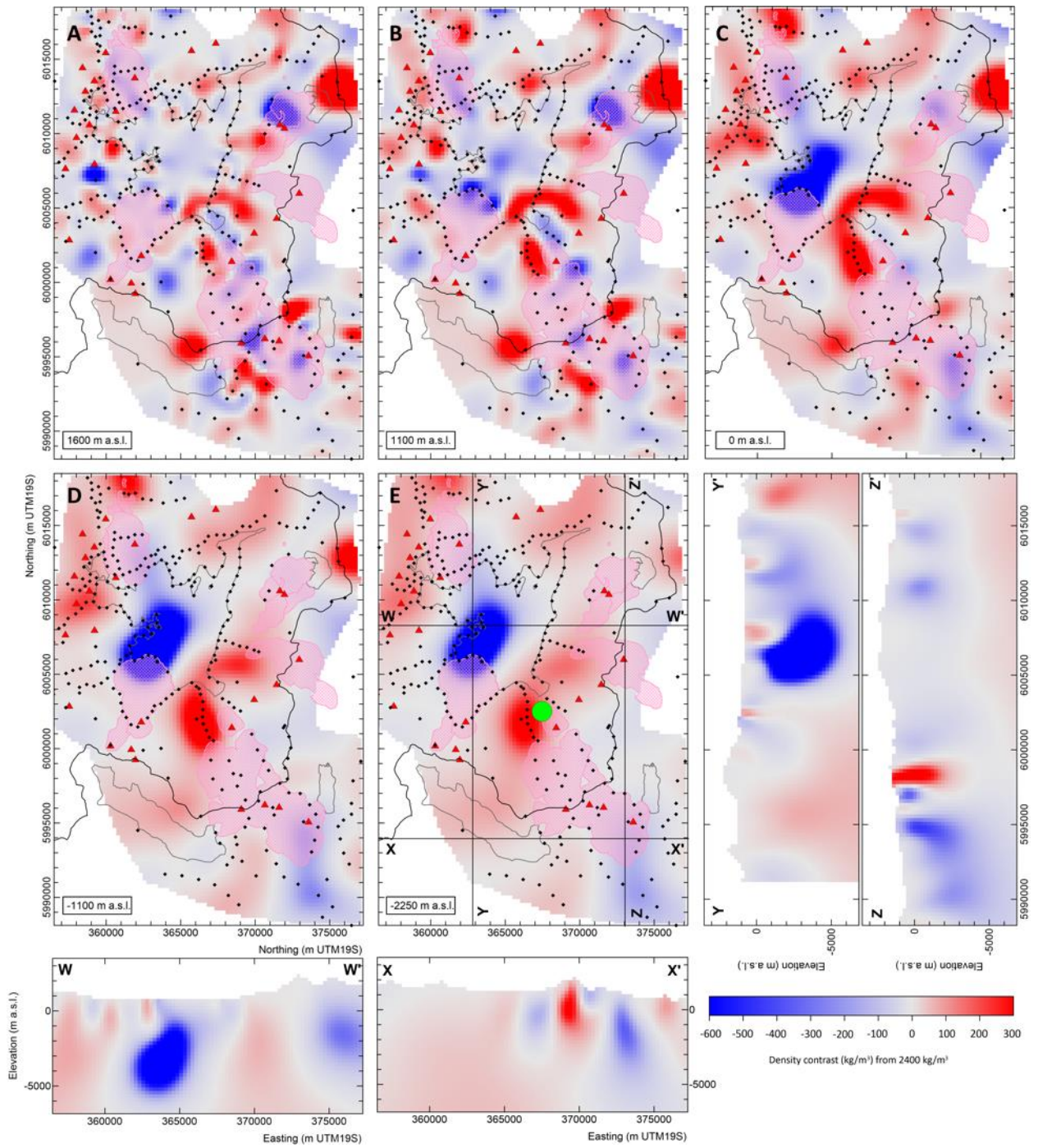
Depth slices at 1600 and 1100 m a.s.l. (Fig. 4A, B) display a patchwork of high- and low-density regions reflecting near surface variations in lithologies (denser lavas vs. thick pyroclastic material). The most significant of these shallow low-density regions is at the eastern end of Laguna Fea (Fig. 5) and represents an accumulation of pyroclastic material that dams the lake.

384 Below 0 m a.s.l the negative density contrast anomalies coalesce into 3 regions: 1) The  
385 Lake anomaly; 2) The Barrancas anomaly and; 3) The Cari Launa and Divisoria anomalies,  
386 although the model is poorly constrained in later area by sparser data coverage. Figure 5 shows  
387 the three-dimensional representation of these bodies as isosurfaces of  $<1900 \text{ kg/m}^3$  (red) and  
388  $2200$  to  $2300 \text{ kg/m}^3$  (grey).

389 The Lake anomaly - identified by Miller et al. (2017b) and Wespestad et al. (2019) - is  
390 interpreted to represent a magma reservoir containing a  $20\text{-}30 \text{ km}^3$  interstitial melt volume  
391 localized within a larger ( $>100 \text{ km}^3$ ) crystal rich mush. In this paper we focus on the  
392 interpretation of the newly identified Barrancas and Cari Launa anomalies.

393 Our model reveals a  $64 \text{ km}^3$  low-density body beneath the ring vent (Fig. 1) on the south-  
394 east part of the Barrancas complex that extends from near surface to 4 km below sea level  
395 beneath which model resolution becomes poor (Fig.4 X-X' and Z-Z' sections). This body has a  
396 maximum density contrast of around  $-220 \text{ kg/m}^3$  or an estimated absolute density of  $2180 \text{ kg/m}^3$ .

397 North of the Barrancas complex, our model reveals a shallower anomaly in the  
398 subsurface beneath the Cari Launa and Divisoria vents that extends to around 2 km below sea  
399 level (Fig 4; W-W' and Z-Z' sections). This  $51 \text{ km}^3$  low-density body is resolved with a density  
400 contrast of  $-100$  to  $-150 \text{ kg/m}^3$  or  $2250$  to  $2300 \text{ kg/m}^3$  absolute density. These anomalies are  
401 poorly constrained by the data due to a lack of measurements from that region.



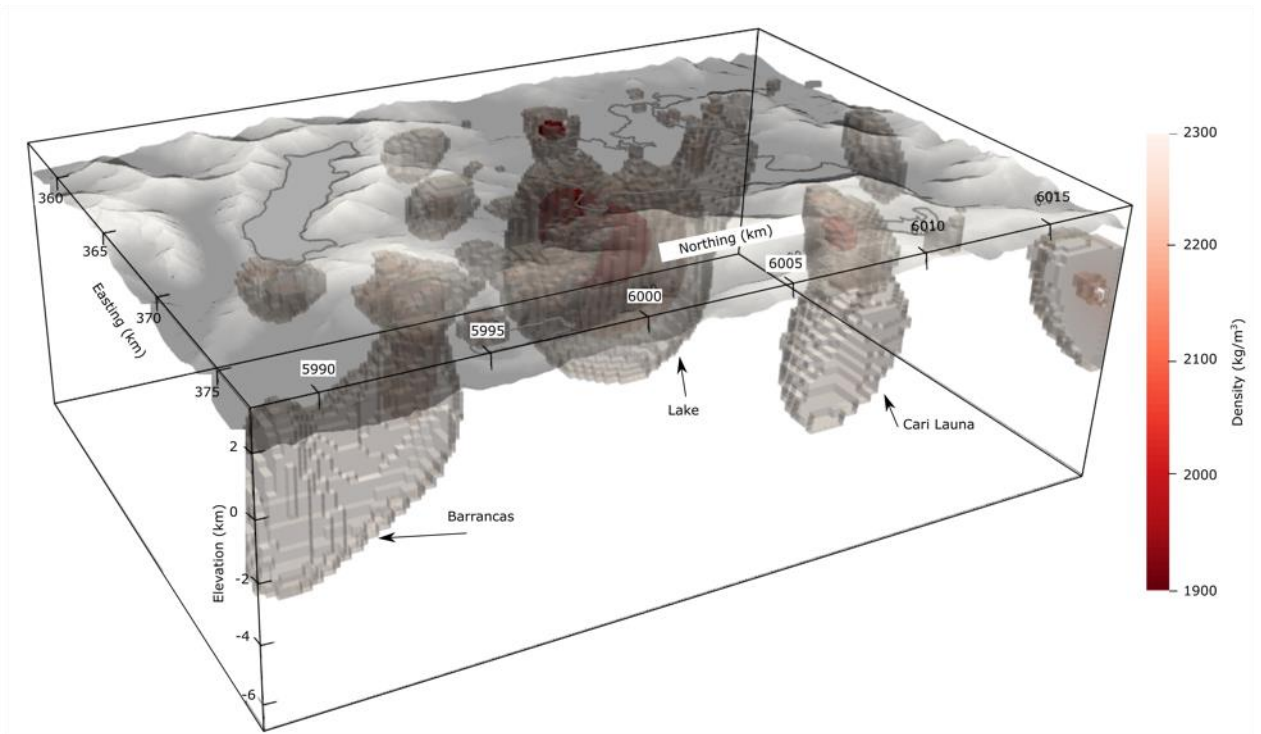
402

403

404

405

**Figure 4.** Depth slices and cross sections from the median inverse model. The green dot is the inferred source of shoreline tilting from Singer et al. (2018).



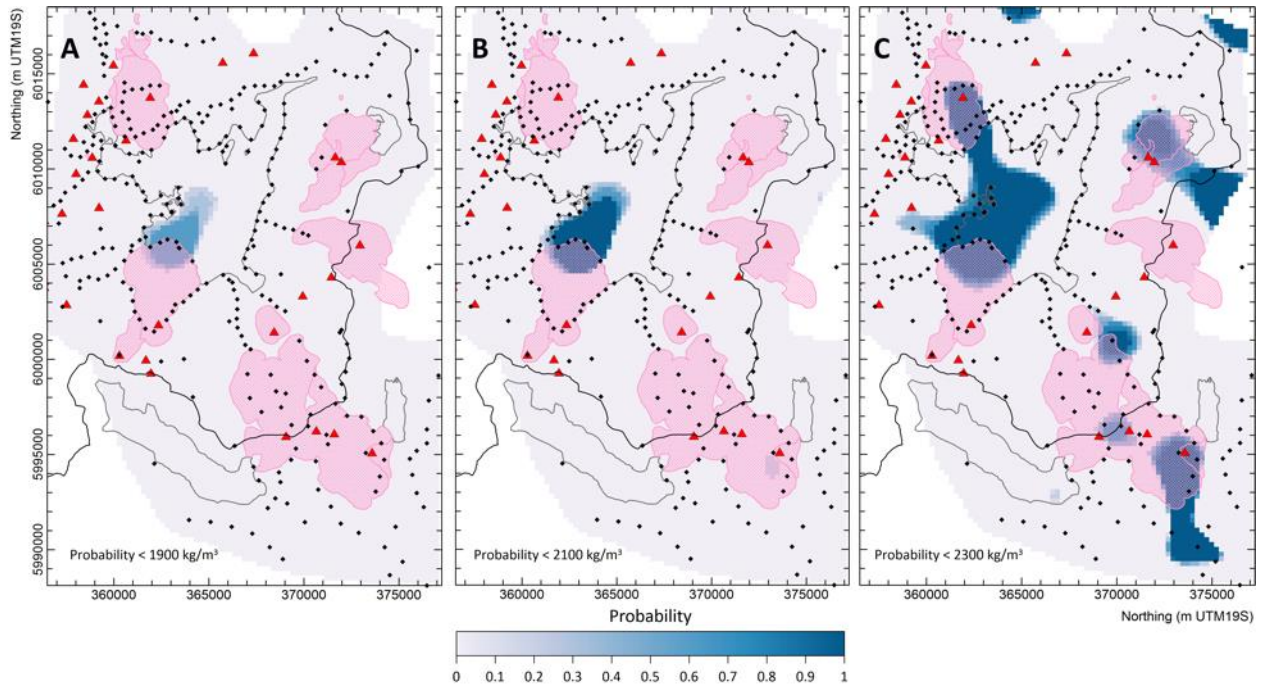
406

407

408 **Figure 5.** Three-dimensional representation of the inverse model showing isosurfaces of  $<1900 \text{ kg/m}^3$   
 409 material (red) and  $2200\text{-}2300 \text{ kg/m}^3$  (grey) material. The Lake low density body is labelled along with the  
 410 Barrancas and Cari Launa bodies. Other smaller bodies have limited depth extent and likely represent shallow  
 411 variations in the thicknesses of pyroclastic deposits. The most important of these is the shallow body at the eastern  
 412 end of Laguna Fea which dams the outlet and poses a flooding hazard should it fail. View is from the south east  
 413 looking to the north west.

414

415 To assess the probability of a specific density value occurring in a model cell, we ran the  
 416 inversion with multiple regularization norms that covered the range of smooth, intermediate, and  
 417 compact models (Fig. 3). From the 10 models, we calculate the probability of a density value  
 418 occurring in each cell and use this information as a measure of confidence in our model. Figure  
 419 6 shows the probabilities of modeled densities.



420

421 **Figure 6.** Probability of a density value occurring in the model, A)  $< 1900 \text{ kg/m}^3$ , B)  
 422  $< 2100 \text{ kg/m}^3$  and C)  $< 2300 \text{ kg/m}^3$ . Depth slice is at 0 m a.s.l. (approximately 2.5 km depth).

423

424 Only the Lake body shows a probability of having a density of  $< 1900 \text{ kg/m}^3$  ( $p=0.6$ ). We  
 425 use the probability descriptors of the IPCC (Mastrandrea et al., 2011) to describe this probability  
 426 as a likely occurrence. The Lake body is virtually certain ( $p>0.99$ ) to have a density of  $< 2100$   
 427  $\text{kg/m}^3$  (Fig. 6B). None of the models indicate material with density  $< 1900 \text{ kg/m}^3$  beneath  
 428 Barrancas or Cari Launa. It is unlikely ( $p=0.2$ ) that material  $< 2100 \text{ kg/m}^3$  exists beneath the  
 429 Barrancas complex, although it is virtually certain ( $p>0.99$ ) that material with density 2100 -  
 430  $2300 \text{ kg/m}^3$  occurs under the south-east corner of the Barrancas complex near the *rng* eruption  
 431 vent. It is also virtually certain ( $p>0.99$ ) that material with 2100 -  $2300 \text{ kg/m}^3$  occurs beneath  
 432 Cari Launa rhyolite flows in the northeast, although the model is poorly constrained in this  
 433 location by sparse data coverage.

434 To test the effect of Bouguer correction density on our residual anomaly data - and hence  
435 inversion models - we re-corrected the gravity data with a correction density of  $2670 \text{ kg/m}^3$  (see  
436 supplementary material). This density is similar to the basement density, but probably too high  
437 for unconsolidated volcanic rocks that comprise the Bouguer slab and terrain above the reduction  
438 ellipsoid. We subtracted a second-order polynomial regional field to create a new residual  
439 gravity anomaly for inversion. Re-running the inversion models with a higher ( $2670 \text{ kg/m}^3$ )  
440 terrain density results in density contrasts beneath Barrancas of  $-300$  to  $-400 \text{ kg/m}^3$ , or absolute  
441 densities of  $2270$  to  $2370 \text{ kg/m}^3$ . In other words, the estimated densities below the Barrancas  
442 complex are similar to the densities obtained using the preferred  $2400 \text{ kg/m}^3$  correction density.  
443 Although derivation of absolute densities from density contrasts beneath the ellipsoid needs to be  
444 done with caution, the density values for the anomalous body beneath Barrancas are very likely  
445 in the range of  $2100$  to  $\sim 2370 \text{ kg/m}^3$ .

## 446 **6 Discussion**

447 Andersen et al. (2017b; 2018; 2019) and Klug et al. (2020) propose a conceptual model  
448 of the LdMVF magma system based on geochronology, whole rock and trace geochemical  
449 distinctions, mineral barometry/thermometry, mineral textures, diffusion chronometry, and melt  
450 inclusion volatile contents. In this model, the sub-LdMVF magma reservoir exists as an  
451 extensive, largely crystalline mush ( $<15\%$  melt) of probable rhyodacitic composition within  
452 which are smaller heterogeneous hot zones of extractable magma ( $25\text{-}50\%$  melt) that contain  
453 discrete pools of eruptible, crystal-poor, rhyolite ( $>85\%$  melt). Critically, these studies identified  
454 two geochemically distinct rhyolite compositions that did not interact with one another; one that  
455 erupted during early post-glacial time, ( $22\text{-}19 \text{ ka}$ ) and another, that includes the Barrancas  
456 complex, that erupted during the Holocene. These two distinct rhyolite magmas may reflect

457 differences in crystal phase proportions in the mush and thermal heterogeneity of the reservoir  
458 with hot zones reflecting regions of variable basaltic intrusion (Andersen et al., 2019). We use  
459 this conceptual petrological model as a framework to interpret and integrate our geophysical  
460 model findings.

461 To constrain our interpretations of the new gravity anomaly data and inversion model, we  
462 used measured densities of rock samples from the exhumed Risco Bayo – Huemul plutonic  
463 complex inferred to represent a frozen analog of a silicic melt storage system. We further  
464 constrain our interpretations with thermodynamic modeling of dacite and rhyolite melt data to  
465 estimate the present-day melt, volatile, and crystal phases beneath the Barrancas complex that  
466 last erupted 2 ka. We investigate if valley filling pyroclastic deposits can account for the  
467 Barrancas anomaly and briefly discuss the effect of hydrothermal activity on our interpretation.  
468 Finally, we discuss the physical interpretation of the density models and implications for magma  
469 storage within the LdMVF, in comparison to previously published findings on the LdMVF  
470 magma system (Miller et al., 2017b; Andersen et al., 2018; Cordell et al., 2018; Wespestad et al.,  
471 2019; Bai et al., 2020; Klug et al., 2020).

472 Our expanded gravity coverage and updated inversion model reveals with high  
473 confidence that the low-density bodies at Barrancas and Cari Launa are discrete from the Lake  
474 gravity anomaly. The Lake anomaly has been previously interpreted as caused by a shallow melt  
475 rich lens within a broader mush (Miller et al., 2017b; Wespestad et al., 2019; Bai et al., 2020).  
476 We focus on the Barrancas anomaly as the Cari Launa anomaly is poorly resolved by our dataset.

477 The Barrancas gravity low (Fig. 2) partially coincides with a 60 – 120 m thick block and  
478 ash flow deposit from the 11.5 ka eruption, which filled the valley south of the edifice (Sruoga et  
479 al., 2015; 2018) (Fig. 1). We calculated the gravity effect of the pyroclastic deposit using a

480 simple two-dimensional model of a 120 m deep, 2 km wide V-shaped valley, filled with material  
481 having a density contrast of  $-400 \text{ kg/m}^3$  which results in a  $-1.6 \text{ mGal}$  anomaly. The absolute  
482 density of the valley fill (approximately  $2000 \text{ kg/m}^3$ ) is the same as used to model the shallow  
483 infill from the 1.8 ka Taupo caldera eruption (Davy & Caldwell, 1998) and is the same as the  
484 average bulk density of 106 samples measured from the 2.36 ka Mt Meagre block and ash flow  
485 (Michol et al., 2008). To recreate the magnitude of the observed anomaly requires filling a  
486 valley 600 m deep or for the density of the material to be around  $900 \text{ kg/m}^3$ ; both parameters are  
487 considered unrealistic. Further, the valley filling model does not reflect the longer wavelengths  
488 of the observed anomaly. Therefore, the entire  $-6 \text{ mGal}$  Barrancas anomaly is not solely due to  
489 thick low-density pyroclastic material.

490 A small ( $> -1$  to  $<1 \text{ mGal}$ ) anomaly immediately west of the Barrancas anomaly is  
491 associated with shallow body of low-density material damming the outlet of Laguna Fea (Fig. 5).  
492 This pumice dam is recognized as a significant hazard to communities living downstream (P.  
493 Sruoga, pers. comm., 2020). There is no stream outlet from Laguna Fea, and via stream piracy  
494 and capture, eventually this pumice dam will likely fail and flood the Barrancas valley.

495 The 62 m upwarping of the Holocene paleoshoreline is inferred by Singer et al. (2018) to  
496 reflect repeated intrusion events below Barrancas. These intrusion events occurred over the last  
497 9.4 ka, at peak rates of  $0.04 \text{ km}^3/\text{year}$ , or an integrated average rate of  $0.0023 \text{ km}^3/\text{year}$  (Singer et  
498 al., 2018). Models of conductive heat loss from plutons formed by repeated magma injection  
499 (e.g., Blundy & Annen, 2016) show that in small high flux systems - such as LdMVF - there  
500 remains significant eruptible melt even 10 ka since the last magma injection. Once the final  
501 magma injection ends, it takes 50-100 ka for the system to first cool to a non-eruptible state ( $<$   
502 approximately 40 % melt) and to finally solidify. Therefore, combined with the recent ( $<2 \text{ ka}$ )

503 and long-lived eruptive history of the Barrancas complex, we interpret this large low-density  
504 body, and the low velocity bodies from seismic tomography, to be remnants of magmatic storage  
505 systems that fed the most recent eruptions between 1 and 2 ka. In the following sections we  
506 discuss the likely state of the magma beneath the Barrancas complex.

### 507 **6.1 Implications of plutonic rock equivalents for gravity anomaly interpretation**

508 The 7.2 to 6.0 Ma Risco Bayo - Huemul plutonic complex was emplaced at 3.7 to 7.2 km  
509 depth and spans a similar range in rock composition as the LdMVF, including crystal-rich  
510 rhyodacites, and the crystal-poor rhyolites that produced the entire Barrancas complex (Schaen et  
511 al., 2017; 2018). Thus, the Risco Bayo and Huemul plutonic rocks provide analogues for  
512 portions of the magma reservoir underlying the LdMVF.

513 Relative to metamorphosed basement rocks, granites commonly yield negative Bouguer  
514 anomalies (e.g., Cordell et al., 1985; Gaynor et al., 2019) if the Bouguer correction (i.e.,  
515 surrounding crustal) density is approximately 2600-2700 kg/m<sup>3</sup>. Metamorphosed basement  
516 rocks in the Chilean Central Andes near Laguna del Maule are typically at 2-3 km depth (Godoy  
517 et al., 1999) and have densities of approximately 2700 kg/m<sup>3</sup>. Overlying these basement rocks  
518 are sedimentary and volcanic rock packages of density between 2300 and 2600 kg/m<sup>3</sup>, consistent  
519 with the correction density obtained for the Laguna del Maule and Barrancas area of 2400 kg/m<sup>3</sup>.  
520 If frozen plutonic bodies of similar composition and density to the Risco Bayo and Huemul  
521 plutons were present at shallow depth (2-3 km) beneath Barrancas, they would create a small  
522 positive Bouguer anomaly, relative to our correction density of 2400 kg/m<sup>3</sup>. If the density of the  
523 crust increases with depth, then these granites would produce neutral or negative anomalies.

524 The lowest density rocks of the exhumed Risco Bayo and Huemul plutonic complex that  
525 represent “frozen melt” have an average density of 2439±15 kg/m<sup>3</sup> (section 2.1) similar to the

526 Bouguer correction density. This density is higher than the density values returned by the  
527 inversion model for the body beneath the Barrancas complex ( $2180 \text{ kg/m}^3$ ) and suggests that the  
528 Barrancas body cannot be a cold, solidified pluton. Rather, it may contain some percent melt  
529 and perhaps an exsolved volatile phase, as also inferred from the slowing of seismic waves  
530 through this region (Wespestad et al., 2019, Bai et al., 2020), and the high  $\text{H}_2\text{O}$  contents of the  
531 rhyolitic melts (Klug et al., 2020). We therefore propose that the low-density body beneath the  
532 Barrancas complex is a combination of low-density surface lavas and pyroclastic material, and a  
533 deeper remnant magma storage system that contains some proportion of residual melt left over  
534 from the last eruption at 1-2 ka. We investigate this hypothesis in the following section using  
535 MELTS thermodynamic modelling tool.

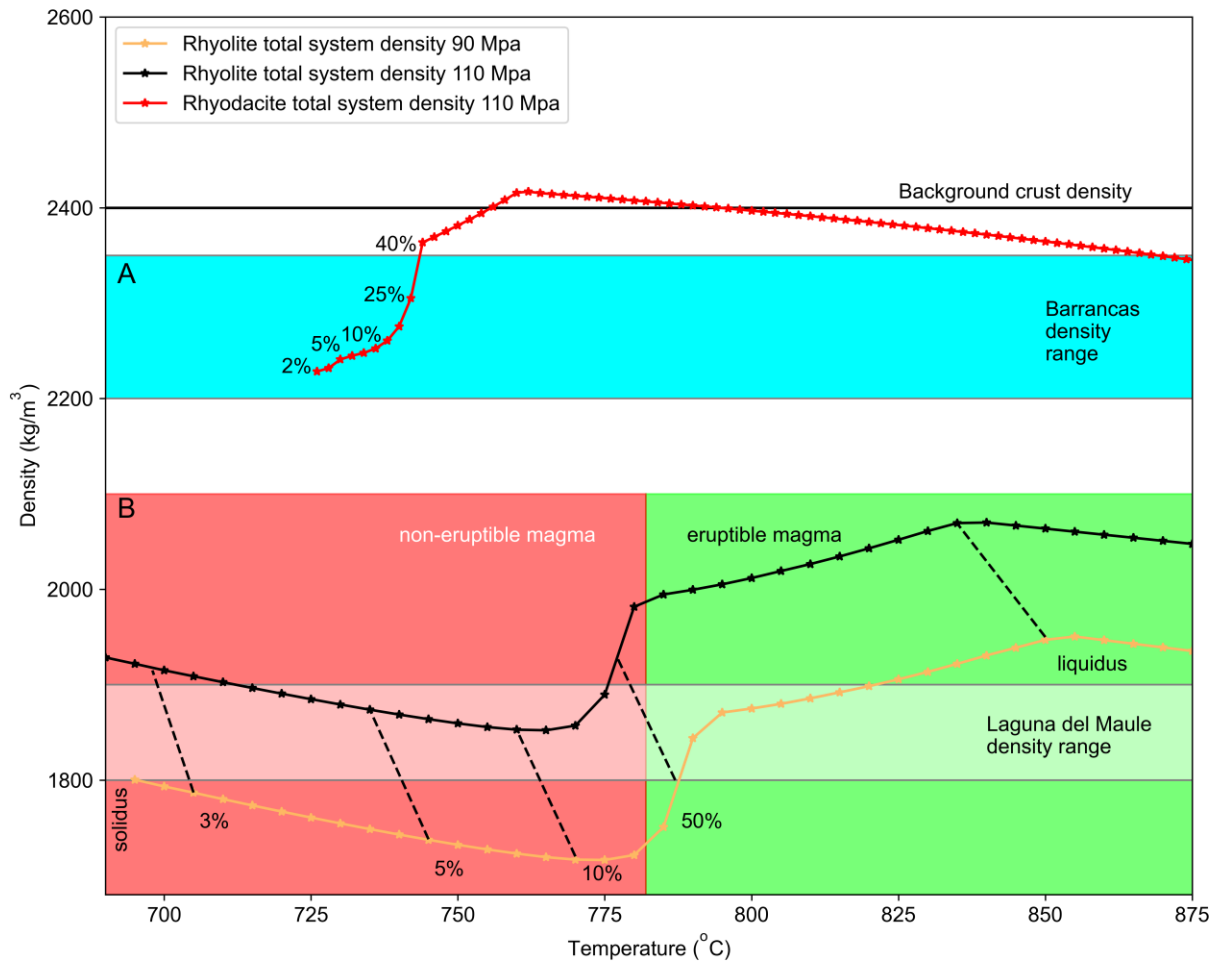
## 536 **6.2 Thermodynamic models and density anomalies**

537 Our gravity model of the Barrancas complex - constrained by independent density  
538 measurements, cooling models, and seismic tomography evidence - suggests that a melt phase is  
539 present in the storage system at 3-4 km depth. To further investigate the presence of melt or  
540 fluid phases within the modeled low-density body beneath the Barrancas complex, we use  
541 Rhyolite MELTS for Excel (Gualda & Ghiorso, 2015) to construct phase diagrams that relate  
542 magma density (melt, crystal, and fluid phases) to temperature and pressure. The magma body is  
543 assumed to be a crystal-rich mush of andesitic to dacitic bulk composition, which contains  
544 volumetrically minor interstitial rhyodacitic to rhyolitic melt. Within the relatively cool upper  
545 crust, this is a more likely state for long-term storage and incubation of silicic magma than a  
546 large, long-lived body of rhyolitic melt (Cooper & Kent, 2014; Andersen et al., 2018). Andersen  
547 et al. (2018) show that for a dacite magma at 200 MPa (ca. 8 km depth), using the external  
548 volatile flux model, a density of  $2200\text{-}2300 \text{ kg/m}^3$  can be produced with less than 10% exsolved

549 fluid volume fraction at a temperature of around 750°C. This is consistent with the high H<sub>2</sub>O  
550 content of melt inclusions and volatile saturation of most rhyolite erupted within the LdMVF  
551 (Klug et al., 2020). However, unlike these rhyolites the Barrancas domes show evidence of  
552 hydrothermal alteration and collapse to produce a large pyroclastic flow, in which melt  
553 inclusions contain little CO<sub>2</sub> and low H<sub>2</sub>O contents (Klug et al., 2020). These features are  
554 interpreted by Klug et al. (2020) to reflect much shallower emplacement (50-100 MPa; less than  
555 4 km depth) and extensive degassing of rhyolitic magma prior to eruption.

556 To model the densities of residual magmas that equilibrate at low pressures and lose  
557 volatiles, simulating conditions thought to occur beneath the Barrancas complex, we use the  
558 rhyodacite of Laguna sin Puerto containing 69% silica, 2.5% H<sub>2</sub>O and no CO<sub>2</sub> (Hildreth et al.,  
559 2010; Klug et al., 2020) as a starting composition. We normalize the composition to retain the  
560 H<sub>2</sub>O phase within the melt and then cool the magma to its solidus at a constant pressure of 110  
561 MPa. The modeled values allow us to track density changes as the magma cools and crystallizes  
562 (Fig. 7A). The liquidus is ~960 °C (not shown on the plot) and as cooling occurs the magma  
563 density rises to a peak of 2420 kg/m<sup>3</sup> at 762 °C. At these conditions, quartz begins to crystallize  
564 and at 760 °C the H<sub>2</sub>O begins to exsolve, lowering the density. Between 744 and 742 °C, with  
565 40 % melt remaining, the exsolved fluid phase doubles in mass from 0.64 to 1.31 wt. % at which  
566 point the density drops further. The density range of Barrancas gravity models span from 2200 -  
567 2350 kg/m<sup>3</sup> matching conditions that include the solidus and up to ~30 % melt plus exsolved  
568 H<sub>2</sub>O (Fig. 7A). In contrast, Figure 7B shows the total system densities of a LdMVF rhyolite  
569 containing 5 wt. % H<sub>2</sub>O at 90 and 110 MPa, with the expected pressure at the approximate depth  
570 range (2.5-3.5 km) of the Lake body imaged by the gravity inversion and teleseismic  
571 tomography. Five weight % H<sub>2</sub>O is likely a minimum, as melt inclusions contain up to 8 wt.%

572 H<sub>2</sub>O (Klug et al., 2020) that would further lower the density. The latter MELTS model replicates  
 573 the densities recovered by the gravity inversion for the Lake anomaly (1800 to 1900 kg/m<sup>3</sup>). To  
 574 reproduce the model densities required for Lake anomaly, the magma system must contain an  
 575 exsolved fluid phase, although the proportion of melt is less certain. A lower bound of 5-14 %  
 576 melt is obtained by coarser gridded seismic tomography models (Wespestad et al., 2019, Bai et  
 577 al., 2020), while the closer spaced gravity data suggests small pockets with ~50 % melt is  
 578 possible in parts of the system depending on the pressure.  
 579



580  
 581 **Figure 7.** Plots of density as a function of temperature estimated by rhyolite MELTS simulations. In both plots the  
 582 annotated percentages indicate melt percent. A) Total system densities (crystal, melt, volatile) of rhyodacite magma

583 containing 2.5% H<sub>2</sub>O (red). The range of densities from the gravity inversion model at Barrancas are shaded light  
584 blue. B) Total system densities of rhyolite magma at 90 and 110 MPa (approx. 2.5 to 4.5 km depth) with melt  
585 proportions (dashed lines). The range of densities from the inversion model of the Lake anomaly are shaded grey.  
586 Eruptible versus non-eruptible magma is shaded red and green around the approximately 50 melt percent  
587 temperature.

### 588 **6.3 Effect of hydrothermal activity**

589 Miller et al. (2017a) proposed that gravity changes associated with the Lake anomaly in  
590 the top 2 km are caused by the influx of hydrothermal fluids into the Troncoso fault zone. As  
591 our modelled low-density bodies extend close to the surface, we consider whether the top portion  
592 of these bodies may in fact represent a rock hosted hydrothermal system as suggested by  
593 Andersen et al. (2018) to explain in part the low densities observed. In a liquid-dominated  
594 hydrothermal system within a porous rock, pore space initially filled by air is replaced by brine  
595 resulting in a small gravity increase. Hence, the presence of an active liquid-dominated  
596 hydrothermal system would slightly increase the observed gravity relative to the surrounding  
597 area.

598 The Barrancas domes show widespread evidence for advanced argillic alteration caused  
599 by circulation of > 300° C fluids during the Holocene (Sruoga et al., 2015). Hydrothermal  
600 alteration can often lower the density of rock (e.g., Miller & Williams-Jones, 2016), although the  
601 magnitude of the density decrease from alteration is typically 1-2 mGal and not enough to  
602 explain the gravity lows observed. MT models of the Barrancas area (Cordell et al., 2018) show  
603 a small shallow (1-2 km) conductive anomaly (10 Ωm) near the summit of Barrancas that may be  
604 consistent with conductive clay minerals formed by hydrothermal alteration. However, the  
605 gravity anomaly extends far south from the altered domes. As such, hydrothermal alteration is  
606 likely to play only a minor part in the observed gravity anomaly.

**6.4 Present state of the Barrancas and broader Laguna del Maule magma reservoir**

Our interpretation of the density model of the LdMVF is partially constrained by equivalent plutonic rocks from the nearby Risco Bayo – Huemul pluton that represent a “frozen” analog. These rocks have densities  $> 2400 \text{ kg/m}^3$ , which would result in positive gravity anomalies if they existed in our residual anomaly map. We note that positive gravity anomalies exist in the older, northern part of the volcanic field suggesting they may represent the cold, frozen portions that may have become plutons. A ridge of positive gravity anomaly divides the Lake anomaly from the Barrancas anomaly. The inversion model indicates that this ridge is a shallow feature extending towards the surface and may represent a buried sequence of Pliocene andesitic lavas comprising the Cola de Zorro Formation within the uppermost 2 km (Hildreth et al., 2010), as opposed to a frozen pluton.

Our new density model of the broader LdMVF has captured what we interpret as at least two magma bodies at different stages of maturity. The large low-density body beneath the Lake represents an active melt storage system containing a substantial free volatile phase, driven by deeper injection of basalt, supplying heat and volatiles and propelling the present-day uplift (Le Mével et al., 2016; Zhan et al., 2019; Klug et al., 2020). The depth of the reservoir is consistent with melt inclusion derived pressure estimates (Klug et al., 2020) and suggests that gravity is imaging the top portion of a trans-crustal magmatic system that extends to  $>25 \text{ km}$  depth (Andersen et al., 2017b; Cordell et al., 2018; Bai et al., 2020). The geochemical data indicate spatially and petrologically discrete magma bodies have persisted during at least the last 25 ka, producing rhyolite eruptions. This data suggest that the multiple discrete bodies captured in the present-day geophysical models are the norm, rather than the exception, at the LdMVF.

Given the spatial coincidence of the teleseismic low- $V_p$  anomaly and the Lake gravity anomaly, joint inversion of the two, either via structural gradients or by analytic relationships

631 that link  $V_p$  and density, is likely to yield greater insight into the physical properties of this  
632 magma body, with ramifications for its present state and future trajectory.

633 The newly discovered Barrancas magma body represents the still warm remains of a  
634 magma body within the reservoir that last erupted 1-2 ka. The melt content is uncertain, but it is  
635 likely to be  $< 30\%$ ; further, it may contain  $< 2.5\%$  volatile phase and is thus in a non-eruptible  
636 condition. This interpretation is consistent with the low  $H_2O$  and  $CO_2$  contents and low  
637 emplacement pressures (50 – 100 MPa) from melt inclusions in the 11.5 ka Barrancas pyroclastic  
638 flow deposit (Klug et al., 2020), suggesting that the magma was thoroughly outgassed prior to its  
639 endogenous and exogenous emplacement as a dome complex at very shallow depths. The Melts  
640 models also suggest that the Barrancas magma body could be at solidus temperatures. However,  
641 the surface wave and teleseismic tomography (Wespestad et al., 2019; Bai et al., 2020)  
642 anomalies - although on the edge of the seismic array - imply some degree of melt remains. Melt  
643 contents inferred by teleseismic tomography suggests the body beneath Barrancas volcanic field,  
644 by comparison to the Lake low VP anomaly, has  $< 14\%$  melt. The deeper portion of the low-  
645 density body under Barrancas may represent the cooling, volatile-depleted, cumulate framework  
646 of a dacitic magma body, which was once the “warm storage” source of rhyolite melt (Anderson  
647 et al., 2017).

648 One possible end point in the development of the Barrancas magma is the formation of a  
649 high silica pluton, similar to the exhumed Huemul pluton to the west of the LdMVF. However,  
650 future injection of basalt beneath the Barrancas complex, as is postulated to be occurring beneath  
651 the Lake anomaly, could reactivate this magma body and continue to drive the paleoshoreline  
652 upwarping observed since 9.4 ka. This scenario is supported by petrochronologic evidence from  
653 the Barrancas complex (Andersen et al., 2019), which suggests that the erupted rhyolites were

654 sourced from a long lived “warm” part of the magma reservoir. This magma reservoir  
655 experienced external additions of heat and volatiles that remobilized interstitial melt shortly prior  
656 to successive eruptions.

## 657 **7 Conclusions**

658 The new residual gravity anomaly map of the LdMVF shows a -6 mGal gravity low  
659 extending from the summit of the Barrancas complex to 5 km southeast of the summit at depth.  
660 The inversion model of the Barrancas anomaly shows a 64 km<sup>3</sup> body dipping to the south east at  
661 a depth of 2-4 km (sea level to 2 km below sea level) with a modelled density of ~2200 to 2350  
662 kg/m<sup>3</sup>. Our interpretation - guided by measured densities from the nearby Risco Bayo - Huemul  
663 plutonic rocks, thermodynamic modeling, and petrologic observations - is that the Barrancas low  
664 density body represents a volatile poor magma with a <30 % melt proportion. This interpretation  
665 is consistent with the presence of magma that degassed at depths less than 3-4 km and produced  
666 domes comprising the Barrancas volcanic complex. We propose this magma represents the  
667 cooling remnant of a once active melt pocket that last erupted 1-2 ka. Moreover, the growth of  
668 this magma reservoir in the shallow crust is likely responsible for the >60 m uplift of the  
669 paleoshoreline in the southern part of the LDM basin since 9.4 ka.

670 Our new geophysical observations of the location, geometry, and state of the magmatic  
671 anomalies in the SE basin provide geophysical evidence that integrates with petrological models  
672 of melt storage. The Barrancas gravity anomaly represents a rhyodacite melt stored in the  
673 shallow crust in warm zones that can be melted, differentiated, extracted, and erupted.  
674 Thermodynamic modelling shows that these bodies may transition from moribund to melt rich  
675 over a relatively small temperature range. Such as temperature increase could result from basalt

676 intrusion, proposed as a mechanism for the present-day inflation above the Lake anomaly (e.g.,  
677 Le Mével et al., 2016).

678 The new gravity model of the LdMVF corroborates extensive petrologic findings and  
679 provides geophysical evidence for at least two separate magma bodies within the same volcanic  
680 field. The emerging picture is one in which a broader magma reservoir can coevally host  
681 multiple melt-bearing domains in differing physical states. This finding has important  
682 implications for future hazard monitoring of the LdMVF, in both Chile and Argentina, as the  
683 Barrancas complex straddles this border.

684

### 685 **Acknowledgements**

686 The Barrancas volcanic field is located at the crest of the Andes, on the border of  
687 Argentina and Chile. Sebastian Garcia and Alvaro Amigo were critical in working with their  
688 respective governments to allow us to complete this fieldwork; and Felipe Diaz acted as the  
689 liaison of the helicopter company with the government agencies. Our sincere thanks to all of  
690 them. Peter Sobol provided logistical support in the field. We gratefully acknowledge the  
691 patience and tenacity of field assistants Eve Meltzer, Jake Klug, and Claire Ruggles. Thanks to  
692 Nicolas Garibaldi for providing samples of the Risco Bayo and Huemul plutons and to Luis  
693 Torres for accommodation and support in Chile. Emily Mixon provided help with the Melts  
694 model work. Kurt Feigl provided funds from his portion of LdM funding for the helicopter time  
695 that allowed the fieldwork to happen. We thank the entire Laguna del Maule research team for  
696 thoughtful and constructive conversations that contributed to this paper. Gravity data are  
697 available from [https://figshare.com/articles/Gravity\\_data\\_from\\_Laguna\\_del\\_Maule/12479981](https://figshare.com/articles/Gravity_data_from_Laguna_del_Maule/12479981).  
698 This study was supported by NSF grant EAR-1411779. Craig Miller is supported by New

699 Zealand government, Ministry of Business, Innovation and Employment, SSIF funding, under  
700 the Volcano Hazards and New Zealand Geothermal programs.

701

### 702 **Author Contributions**

703 ST coordinated and participated in data collection, processing, and analysis of the  
704 Barrancas dataset. CM ran the inversion models and led the analysis and writing of the  
705 manuscript. BT conceived the project, organized the fieldwork, and participated in field work in  
706 Chile and Argentina, and assisted in data processing and analysis. DF ran the synthetic model  
707 and provided the code for the inversion models. BSS initiated the integrative study of Laguna  
708 del Maule, obtained the funding, established a collaboration with SERNAGEOMIN, facilitated  
709 permission for the helicopter work in the border area, and provided the petrologic context. All  
710 authors provided critical review and editing of the final manuscript.

711

### 712 **References**

- 713 Andersen, N. L., Jicha, B. R., Singer, B. S., & Hildreth, W. (2017a). Incremental heating of  
714 Bishop Tuff sanidine reveals preeruptive radiogenic Ar and rapid remobilization from cold  
715 storage. *Proceedings of the National Academy of Sciences*, 201709581.  
716 <https://doi.org/10.1073/pnas.1709581114>
- 717 Andersen, N. L., Singer, B. S., Jicha, B. R., Beard, B. L., Johnson, C. M., & Licciardi, J. M.  
718 (2017b). Pleistocene to Holocene Growth of a Large Upper Crustal Rhyolitic Magma  
719 Reservoir beneath the Active Laguna del Maule Volcanic Field, Central Chile. *Journal of*  
720 *Petrology*, 58(1), 85–114. <https://doi.org/10.1093/petrology/egx006>
- 721 Andersen, N. L., Singer, B. S., Costa, F., Fournelle, J., Herrin, J. S., & Fabbro, G. N. (2018).

- 722 Petrochronologic perspective on rhyolite volcano unrest at Laguna del. *Earth and Planetary*  
723 *Science Letters*, 493, 57–70. <https://doi.org/10.1016/j.epsl.2018.03.043>
- 724 Andersen, N. L., Singer, B. S., & Coble, M. A. (2019). Repeated Rhyolite Eruption From  
725 Heterogeneous Hot Zones Embedded Within a Cool, Shallow Magma Reservoir. *Journal of*  
726 *Geophysical Research: Solid Earth*, 124(3), 2582–2600.  
727 <https://doi.org/10.1029/2018JB016418>
- 728 Bachmann, O., Miller, C. F., & de Silva, S. L. (2007). The volcanic-plutonic connection as a  
729 stage for understanding crustal magmatism. *Journal of Volcanology and Geothermal*  
730 *Research*, 167(1–4), 1–23. <https://doi.org/10.1016/j.jvolgeores.2007.08.002>
- 731 Bachmann, Olivier, & Bergantz, G. (2008). The magma reservoirs that feed supereruptions.  
732 *Elements*, 4(1), 17–21. <https://doi.org/10.2113/GSELEMENTS.4.1.17>
- 733 Bai, T., Thurber, C., Lanza, F., Singer, B. S., Bennington, N., Keranen, K., & Cardona, C.  
734 (2020). Teleseismic tomography of the Laguna del Maule Volcanic Field in Chile. *Journal*  
735 *of Geophysical Research: Solid Earth*. <https://doi.org/10.1029/2020JB019449>
- 736 Barboni, M., Boehnke, P., Schmitt, A. K., Mark Harrison, T., Shane, P., Bouvier, A. S., &  
737 Baumgartner, L. (2016). Warm storage for arc magmas. *Proceedings of the National*  
738 *Academy of Sciences of the United States of America*, 113(49), 13959–13964.  
739 <https://doi.org/10.1073/pnas.1616129113>
- 740 Battaglia, M., Poland, M. P., & Kauahikaua, J. (2012). GTools: An interactive computer program  
741 to process gravity data for high resolution applications. In *AGU Fall Meeting* (pp. GP43B-  
742 1143).
- 743 Bertrand, E. A., Caldwell, T. G., Hill, G. J., Wallin, E. L., Bennie, S. L., Cozens, N., et al.

- 744 (2012). Magnetotelluric imaging of upper-crustal convection plumes beneath the Taupo  
745 Volcanic Zone, New Zealand. *Geophysical Research Letters*, 39(2), 1–6.  
746 <https://doi.org/10.1029/2011GL050177>
- 747 Blundy, J. D., & Annen, C. J. (2016). Crustal Magmatic Systems from the Perspective of Heat  
748 Transfer. *Elements*, 12(2), 115–120. <https://doi.org/10.2113/gselements.12.2.115>
- 749 Brocher, T. M. (2005). Empirical Relations between Elastic Wavespeeds and Density in the  
750 Earth's Crust. *Bulletin of the Seismological Society of America*, 95(6), 2081–2092.  
751 <https://doi.org/10.1785/0120050077>
- 752 Cáceres, F., Castruccio, Á., & Parada, M. A. (2018). Morphology, Effusion Rates, and Petrology  
753 of Postglacial Lavas of Laguna del Maule Volcanic Field, Chilean Andes, and Implications  
754 for Their Plumbing System. *Geochemistry, Geophysics, Geosystems*, 19(12), 4925–4944.  
755 <https://doi.org/10.1029/2018GC007817>
- 756 Cockett, R., Kang, S., Heagy, L. J., Pidlisecky, A., & Oldenburg, D. W. (2015). SimPEG: An  
757 open source framework for simulation and gradient based parameter estimation in  
758 geophysical applications. *Computers and Geosciences*, 85, 142–154.  
759 <https://doi.org/10.1016/j.cageo.2015.09.015>
- 760 Comeau, M. J., Unsworth, M. J., Ticona, F., & Sunagua, M. (2015). Magnetotelluric images of  
761 magma distribution beneath Volcán Uturuncu, Bolivia: Implications for magma dynamics.  
762 *Geology*, 43(3), 243–246. <https://doi.org/10.1130/G36258.1>
- 763 Cooper, K. M., & Kent, A. J. R. (2014). Rapid remobilization of magmatic crystals kept in cold  
764 storage. *Nature*, 506(7489), 480–483. <https://doi.org/10.1038/nature12991>
- 765 Cordell, D., Unsworth, M. J., & Díaz, D. (2018). Imaging the Laguna del Maule Volcanic Field,

766 central Chile using magnetotellurics: Evidence for crustal melt regions laterally-offset from  
767 surface vents and lava flows. *Earth and Planetary Science Letters*, 488, 168–180.

768 <https://doi.org/10.1016/j.epsl.2018.01.007>

769 Cordell, D., Unsworth, M. J., Diaz, D., Reyes-Wagner, V., Currie, C. A., Hicks, S. P. (2019)

770 Fluid and melt pathways in the central Chilean subduction zone near the 2010 Maule

771 earthquake (35–36°S) as inferred from magnetotelluric data. *Geochemistry, Geophysics,*

772 *Geosystems* 20(4), 1818-1835.

773 Cordell, D., Unsworth, M. J., Lee, B., Diaz, D., Bennington, N. (2020) Integrating

774 magnetotelluric and seismic images of silicic magma systems: A case study from the

775 Laguna del Maule Volcanic Field, central Chile. *Journal of Geophysical Research: Solid*

776 *Earth*.

777 Cordell, L., Long, C. L., & Jones, D. W. (1985). Geophysical expression of the batholith beneath

778 Questa Caldera, New Mexico. *Journal of Geophysical Research*, 90(4), 11263.

779 <https://doi.org/10.1029/JB090iB13p11263>

780 Davy, B. W., & Caldwell, T. G. (1998). Gravity, magnetic and seismic surveys of the caldera

781 complex, Lake Taupo, North Island, New Zealand. *Journal of Volcanology and Geothermal*

782 *Research*, 81, 69–89. [https://doi.org/10.1016/S0377-0273\(97\)00074-7](https://doi.org/10.1016/S0377-0273(97)00074-7)

783 Druitt, T. H., Costa, F., Deloule, E., Dungan, M., & Scaillet, B. (2012). Decadal to monthly

784 timescales of magma transfer and reservoir growth at a caldera volcano. *Nature*, 482(7383),

785 77–80. <https://doi.org/10.1038/nature10706>

786 Feigl, K. L., Le Mevel, H., Tabrez Ali, S., Cordova, L., Andersen, N. L., DeMets, C., & Singer,

787 B. S. (2014). Rapid uplift in Laguna del Maule volcanic field of the Andean Southern

788 Volcanic zone (Chile) 2007-2012. *Geophysical Journal International*, 196(2), 885–901.

789 <https://doi.org/10.1093/gji/ggt438>

790 Folguera, A., Alasonati Tašárová, Z., Götze, H.-J., Rojas Vera, E., Giménez, M., & Ramos, V. a.  
791 (2012). Retroarc extension in the last 6 Ma in the South-Central Andes (36°S–40°S)  
792 evaluated through a 3-D gravity modelling. *Journal of South American Earth Sciences*, 40,  
793 23–37. <https://doi.org/10.1016/j.jsames.2012.08.003>

794 Garibaldi, N., Tikoff, B., Schaen, A. J., & Singer, B. S. (2018). Interpreting Granitic Fabrics in  
795 Terms of Rhyolitic Melt Segregation, Accumulation, and Escape Via Tectonic Filter  
796 Pressing in the Huemul Pluton, Chile. *Journal of Geophysical Research: Solid Earth*.  
797 <https://doi.org/10.1029/2018JB016282>

798 Gaynor, S. P., Coleman, D. S., Rosera, J. M., & Tappa, M. J. (2019). Geochronology of a  
799 Bouguer Gravity Low. *Journal of Geophysical Research: Solid Earth*, 124(3), 2457–2468.  
800 <https://doi.org/10.1029/2018JB015923>

801 Glazner, A. F., Bartley, J. M., Coleman, D. S., Gray, W., & Taylor, R. Z. (2004). Are plutons  
802 assembled over millions of years by amalgamation from small magma chambers? *GSA*  
803 *Today*, 14(4), 4. [https://doi.org/10.1130/1052-5173\(2004\)014<0004:APAOMO>2.0.CO;2](https://doi.org/10.1130/1052-5173(2004)014<0004:APAOMO>2.0.CO;2)

804 Godoy, E., Yañez, G., & Vera, E. (1999). Inversion of an Oligocene volcano-tectonic basin and  
805 uplifting of its superimposed Miocene magmatic arc in the Chilean Central Andes: First  
806 seismic and gravity evidences. *Tectonophysics*, 306(2), 217–236.  
807 [https://doi.org/10.1016/S0040-1951\(99\)00046-3](https://doi.org/10.1016/S0040-1951(99)00046-3)

808 Gualda, G. A. R., & Ghiorso, M. S. (2015). MELTS\_Excel: A Microsoft Excel-based MELTS  
809 interface for research and teaching of magma properties and evolution.  
810 *Geochemistry, Geophysics, Geosystems*, 16, 315–324.

- 811 <https://doi.org/10.1002/2014GC005545>.Received
- 812 Hildreth, W., Godoy, E., Fierstein, J., & Singer, B. S. (2010). Laguna del Maule volcanic field:  
813 Eruptive history of a Quaternary basalt to rhyolite distributed volcanic field on the Andean  
814 range crest in central Chile. *Servicio Nacional de Geología y Minería, Bolletín*, 63, 145.
- 815 Hinze, W. J., Aiken, C., Brozena, J., Coakley, B., Dater, D., Flanagan, G., et al. (2005). New  
816 standards for reducing gravity data: The North American gravity database. *GEOPHYSICS*,  
817 70(4), J25–J32. <https://doi.org/10.1190/1.1988183>
- 818 Huber, C., Townsend, M., Degruyter, W., & Bachmann, O. (2019). Optimal depth of  
819 subvolcanic magma chamber growth controlled by volatiles and crust rheology. *Nature*  
820 *Geoscience*. <https://doi.org/10.1038/s41561-019-0415-6>
- 821 Klug, J. D., Singer, B. S., Kita, N. T., & Spicuzza, M. J. (2020). Storage and evolution of Laguna  
822 del Maule rhyolites: insight from volatile and trace element contents in melt inclusions.  
823 *Journal of Geophysical Research: Solid Earth*. <https://doi.org/10.1029/2020JB019475>
- 824 Le Mével, H., Feigl, K. L., Cordova, L., Demets, C., & Lundgren, P. (2015). Evolution of unrest  
825 at Laguna del Maule volcanic field ( Chile ) from InSAR and GPS measurements , 2003 to  
826 2014. *Geophysical Research Letters*, 1–24. <https://doi.org/10.1109/36.662741>.Pitz
- 827 Le Mével, H., Gregg, P. M., & Feigl, K. L. (2016). Magma injection into a long-lived reservoir  
828 to explain geodetically measured uplift: Application to the 2007-2014 unrest episode at  
829 Laguna del Maule volcanic field, Chile. *Journal of Geophysical Research: Solid Earth*,  
830 121(8), 6092–6108. <https://doi.org/10.1002/2016JB013066>
- 831 Le Mével, H., Feigl, K. L., Cordova, L., Bekaert, D.P., & Singer, B.S. (2019) Re-accelerating  
832 deformation at Laguna del Maule volcanic field, Southern Andes. *American Geophysical*

- 833 *Union Fall Meeting Abstracts*, 2019AGUFM.G33C0701L
- 834 Magee, C., Stevenson, C. T. E., Ebmeier, S. K., Keir, D., Hammond, J. O. S., Gottsmann, J. H.,  
835 et al. (2018). Magma Plumbing Systems: A Geophysical Perspective. *Journal of Petrology*,  
836 (July), 1–35. <https://doi.org/10.1093/petrology/egy064>
- 837 Mastrandrea, M. D., Mach, K. J., Plattner, G. K., Edenhofer, O., Stocker, T. F., Field, C. B., et al.  
838 (2011). The IPCC AR5 guidance note on consistent treatment of uncertainties: A common  
839 approach across the working groups. *Climatic Change*, 108(4), 675–691.  
840 <https://doi.org/10.1007/s10584-011-0178-6>
- 841 Michol, K. A., Russell, J. K., & Andrews, G. D. M. (2008). Welded block and ash flow deposits  
842 from Mount Meager, British Columbia, Canada. *Journal of Volcanology and Geothermal*  
843 *Research*, 169(3–4), 121–144. <https://doi.org/10.1016/j.jvolgeores.2007.08.010>
- 844 Miller, Craig A, & Williams-Jones, G. (2016). Internal structure and volcanic hazard potential of  
845 Mt Tongariro, New Zealand, from 3D gravity and magnetic models. *Journal of Volcanology*  
846 *and Geothermal Research*, 319, 12–28. <https://doi.org/10.1016/j.jvolgeores.2016.03.012>
- 847 Miller, C. A., Le Mével, H., Currenti, G., Williams-Jones, G., & Tikoff, B. (2017a).  
848 Microgravity changes at the Laguna del Maule volcanic field: Magma-induced stress  
849 changes facilitate mass addition. *Journal of Geophysical Research: Solid Earth*, 122(4),  
850 3179–3196. <https://doi.org/10.1002/2017JB014048>
- 851 Miller, Craig A., Williams-Jones, G., Fournier, D., & Witter, J. (2017b). 3D gravity inversion  
852 and thermodynamic modelling reveal properties of shallow silicic magma reservoir beneath  
853 Laguna del Maule, Chile. *Earth and Planetary Science Letters*, 459, 14–27.  
854 <https://doi.org/10.1016/j.epsl.2016.11.007>

- 855 Nettleton, L. L. (1939). Determination of density for reduction of gravimeter observations.  
856 *Geophysics*, 4(3). <https://doi.org/10.1190/1.1437088>
- 857 Parasnis, D. S. (1966). *Mining Geophysics*. Elsevier, Amsterdam-London-New York.
- 858 Paulatto, M., Moorkamp, M., Hautmann, S., Hooft, E., Morgan, J. V., & Sparks, R. S. J. (2019).  
859 Vertically Extensive Magma Reservoir Revealed From Joint Inversion and Quantitative  
860 Interpretation of Seismic and Gravity Data. *Journal of Geophysical Research: Solid Earth*,  
861 124(11), 11170–11191. <https://doi.org/10.1029/2019JB018476>
- 862 Peterson, D., Garibaldi, N., Keranen, K., Tikoff, B., Miller, C., Lara, L. E., et al. (2020). Active  
863 normal faulting, diking, and doming above the rapidly inflating Laguna del Maule volcanic  
864 field, Chile imaged with CHIRP, magnetic, and focal mechanism data. *Journal of*  
865 *Geophysical Research: Solid Earth*. <https://doi.org/10.1029/2019JB019329>
- 866 del Potro, R., Díez, M., Blundy, J., Camacho, A. G., & Gottsmann, J. (2013). Diapiric ascent of  
867 silicic magma beneath the Bolivian Altiplano. *Geophysical Research Letters*, 40(10), 2044–  
868 2048. <https://doi.org/10.1002/grl.50493>
- 869 Pritchard, M. E., & Gregg, P. M. (2016). Geophysical Evidence for Silicic Crustal Melt in the  
870 Continents: Where, What Kind, and How Much? *Elements*, 12(2), 121–127.  
871 <https://doi.org/10.2113/gselements.12.2.121>
- 872 Represas, P., Catalão, J., Montesinos, F. G., Madeira, J., Mata, J., Antunes, C., & Moreira, M.  
873 (2012). Constraints on the structure of Maio Island (Cape Verde) by a three-dimensional  
874 gravity model: imaging partially exhumed magma chambers. *Geophysical Journal*  
875 *International*, 190(2), 931–940. <https://doi.org/10.1111/j.1365-246X.2012.05536.x>
- 876 Rubin, A. E., Cooper, K. M., Till, C. B., Kent, A. J. R., Costa, F., Bose, M., et al. (2017). Rapid

- 877 cooling and cold storage in a silicic magma reservoir recorded in individual crystals.  
878 *Science*, 1156(June), 1154–1156. <https://doi.org/10.1126/science.aam8720>
- 879 Schaen, A. J., Cottle, J. M., Singer, B. S., Brenhin Keller, C., Garibaldi, N., & Schoene, B.  
880 (2017). Complementary crystal accumulation and rhyolite melt segregation in a late  
881 Miocene Andean pluton. *Geology*, 45(9), 835–838. <https://doi.org/10.1130/G39167.1>
- 882 Schaen, A. J., Singer, B. S., Cottle, J. M., Garibaldi, N., Schoene, B., Satkoski, A. M., &  
883 Fournelle, J. (2018). Textural and Mineralogical Record of Low Pressure Melt Extraction  
884 and Silicic Cumulate Formation in the late Miocene Risco Bayo-Huemul Plutonic Complex,  
885 Southern Andes. *Journal of Petrology*, 59(10), 1991–2016.  
886 <https://doi.org/10.1093/petrology/egy087>
- 887 Singer, B S, Andersen, N. L., Le Mével, H., Feigl, K. L., DeMets, C., Tikoff, B., et al. (2014).  
888 Dynamics of a large, restless, rhyolitic magma system at Laguna del Maule, southern  
889 Andes, Chile. *GSA Today*. <https://doi.org/10.1130/GSATG216A.1>
- 890 Singer, B.S., Le Mével, H., Licciardi, J.M., Córdova, L., Tikoff, B., Garibaldi, N., Andersen,  
891 N.L., Diefenbach, A.K. & Feigl, K.L. (2018). Geomorphic expression of rapid Holocene  
892 silicic magma reservoir growth beneath Laguna del Maule, Chile. *Science advances*, 4(6),  
893 p.eaat1513.
- 894 Sruoga, P., Elissondo, M., Fierstein, J., Garcia, S., Gonzalez, R., & Rosas, M. (2015). Actividad  
895 explosiva postglacial del centro barrancas, complejo volcanico Laguna del Maule. In  
896 *Congreso Geologico Chileno* (pp. 49–52).
- 897 Sruoga, P., Elissondo, M., Rosas, M., Fierstein, J., & Singer, B. S. (2018). Cerro Barrancas,  
898 Laguna Del Maule Volcanic Field, Chile: unraveling its eruptive history to constrain hazard

- 899 assessment. In *AGU Chapman Conference*. AGU. Retrieved from  
900 <https://agu.confex.com/agu/18chapman1/webprogram/Paper328208.html>
- 901 Tašárová, Z. A. (2007). Towards understanding the lithospheric structure of the southern Chilean  
902 subduction zone (36°S-42°S) and its role in the gravity field. *Geophysical Journal  
903 International*, 170(3), 995–1014. <https://doi.org/10.1111/j.1365-246X.2007.03466.x>
- 904 Tikhonov, A. N., & Arsenin, V. Y. (1977). *Solutions of Ill-posed Problems*.
- 905 Till, C. B., Vazquez, J. A., & Boyce, J. W. (2015). Months between rejuvenation and volcanic  
906 eruption at Yellowstone caldera, Wyoming. *Geology*, 43(8), 695–698.  
907 <https://doi.org/10.1130/G36862.1>
- 908 Till, C. B., Pritchard, M. E., Miller, C. A., Brugman, K. K., & Ryan-davis, J. (2018). Super-  
909 volcanic investigations. *Nature Geoscience*. <https://doi.org/10.1038/s41561-018-0100-1>
- 910 Uieda, L. (2018). Verde: Processing and gridding spatial data using Green’s functions. *Journal  
911 of Open Source Software*, 3(30), 957. <https://doi.org/10.21105/joss.00957>
- 912 Wespestad, C. E., Thurber, C. H., Andersen, N. L., Singer, B. S., Cardona, C., Zeng, X., et al.  
913 (2019). Magma Reservoir Below Laguna del Maule Volcanic Field, Chile Imaged with  
914 Surface-Wave Tomography. *Journal of Geophysical Research: Solid Earth*, 1–15.  
915 <https://doi.org/10.1029/2018JB016485>
- 916 Zhan, Y., Gregg, P. M., Le Mével, H., Miller, C. A., & Cardona, C. (2019). Integrating Reservoir  
917 Dynamics, Crustal Stress, and Geophysical Observations of the Laguna del Maule  
918 Magmatic System by FEM Models and Data Assimilation. *Journal of Geophysical  
919 Research: Solid Earth*, 124(12), 13547–13562. <https://doi.org/10.1029/2019JB018681>
- 920